VOLCANICA Article in Press

This is an uncorrected proof, meaning that this manuscript has not been copyedited or formatted according to Volcanica's styles and standards. In turn, this means that article content, including text, may still change prior to final publication. Although articles in press do not have all bibliographic details available yet, they can be cited using the year of online publication and the DOI, as follows: author(s)(year), article title, Volcanica, DOI.

Permana, T., Suryanto, W., Irnaka, T. M., Darmawan, H., Anggraini, A., Yuliantoro, P., Santoso, A. B. and Weber, B. (2026) "Evaluating seismicity monitoring at Merapi Volcano using a Raspberry Shake RS&BOOM array at a suboptimal distance", *Volcanica*, 9(2). doi: 10.30909/vol/alrm3722.

article in press

Evaluating seismicity monitoring at Merapi Volcano using a Raspberry Shake RS&BOOM array at a suboptimal distance

Theodorus Permana*[1], Wiwit Suryanto[1], Theodosius Marwan Irnaka[1], Herlan Darmawan[1], Ade Anggraini[1], Pamungkas Yuliantoro[1], Agus Budi Santoso[2], and Bernd Weber[3]

[1] Seismology, Volcanology, and Disaster Hazards Research Group, Department of Physics, Faculty of Mathematics and Natural Sciences, Universitas Gadjah Mada, Sleman, DI Yogyakarta 55281, Indonesia

[2] Balai Penyelidikan dan Pengembangan Teknologi Kebencanaan Geologi (BPPTKG), Kota Yogyakarta, DI Yogyakarta 55166, Indonesia

[3] gempa GmbH, Heinrich-Mann-Allee 18/19, Potsdam 14473, Germany

* theopermana@ugm.ac.id [corresponding author]

ORCiD (1st author): 0000.0002.1507.9212

ORCiD (2nd author): 0000.0002.6275.7880

ORCiD (3rd author): 0000.0002.0040.5142

ORCiD (4th author): 0000.0001.6166.8272

ORCiD (5th author): 0000.0002.3942.3460

Keywords: Volcano seismology; Volcano monitoring; Volcanic earthquake; Seismic array; Merapi; Raspberry

article in press

Abstract

Low-cost instruments increasingly complement volcano monitoring where proximal deployments are limited by cost, access, or safety. Practical deployments may occupy suboptimal sites farther from the volcano, where weak volcanic signals and local noise reduce performance. We evaluated what remains recoverable from a five-station Raspberry Shake RS&BOOM array installed approximately 17 km from Merapi, Indonesia. Using June-December 2023 continuous data, we developed a median-based detection and array-characterization approach using apparent velocity, back-azimuth stability, back-azimuth-derived weight, and an elevation-based parameter. The 0.8-1.8 Hz band suppressed microseismic and anthropogenic noise but limited sensitivity to broader-band events. The analysis produced 1,677 detections: 637 (37.98%) matched the official catalogue and 1,036 (61.78%) remained unclassified. Match rates reached 80.80% for tectonic events, 27.78% for pyroclastic flows, and 23.86% for VT-B events, but were <1% for MP, LF, and rockfall events. The array cannot replace proximal monitoring, but provides a constrained benchmark for distant low-cost deployments.

Intisari (Bahasa Indonesia)

Instrumen berbiaya rendah semakin banyak digunakan untuk melengkapi pemantauan gunung api ketika penggunaan stasiun proksimal dibatasi oleh biaya, akses, atau keselamatan. Namun, pemasangannya sering dipaksa pada lokasi suboptimal yang lebih jauh dari gunung api, sehingga sinyal vulkanik yang lemah dan derau lokal dapat menurunkan kinerja pemantauan. Studi ini mengevaluasi informasi yang masih dapat diperoleh dari array yang terdiri dari lima Raspberry Shake RS&BOOM yang dipasang sekitar 17 km dari Gunung Merapi. Data kontinu selama Juni-Desember 2023 dianalisis dengan deteksi berbasis median dan karakterisasi array menggunakan kecepatan semu, kestabilan back-azimuth, bobot dari back-azimuth, dan parameter berbasis elevasi. Rentang frekuensi 0,8-1,8 Hz menekan derau mikroseismik dan antropogenik, tetapi membatasi sensitivitas terhadap kejadian dengan rentang frekuensi lebar. Analisis menghasilkan 1.677 deteksi: 637 (37,98%) cocok dengan katalog resmi dan 1.036 (61,78%) tidak terklasifikasi. Tingkat kecocokan mencapai 80,80% untuk tektonik, 27,78% untuk awan panas, dan 23,86% untuk VT-B, tetapi <1% untuk MP, LF, dan guguran.

Introduction

Monitoring volcanic activity, particularly for hazard assessment, early warning, and disaster mitigation, typically requires deploying instruments in close proximity to the volcano of interest. In the context of seismic monitoring, the main objectives are to observe, detect, and locate various types of seismic events. These events can differ in duration, amplitude, and frequency, each reflecting distinct physical processes within the volcano, often associated with the movement of volcanic fluids such as magma, gas, and water (Nishimura and Iguchi 2011; Zobin 2016). The ability to track temporal changes in the characteristics and source locations of such seismic events is therefore essential for understanding the evolution of volcanic activity, particularly those that may precede or accompany eruptions. In addition, seismic observations can provide constraints on the internal structure of a volcano (Hidayati et al. 2007; Journeau et al. 2022). To achieve these goals, seismometers should ideally be distributed around the volcano to ensure good azimuthal coverage and spatial resolution (Ogiso and Tamaribuchi 2022; Walsh et al. 2017). Merapi Volcano provides a suitable target for evaluating monitoring strategies because it combines high volcanic hazard, complex tectonic setting, dense surrounding population, and the availability of reference observations from an established monitoring network. Located in Central Java, Indonesia, Merapi lies within the tectonically active Sunda arc, where the Indo-Australian Plate subducts beneath the Eurasian Plate along the Sunda-Java Trench at a convergence rate of approximately 67 mm/year (Fig. 1a) (Hutchings and Mooney 2021). This subduction system

article in press

defines the regional tectonic framework, producing a north-dipping Benioff zone and a chain of active volcanoes, including Merapi, as part of the Sunda volcanic arc (Hutchings and Mooney 2021; Irsyam et al. 2017). An inferred NW–SE-trending crustal fault passes through Merapi, while another active NE–SW-oriented structure, the Opak Fault, lies near Yogyakarta, a major population centre close to the volcano (Fig. 1b) (Saputra et al. 2021). Together, these structures reflect the complex upper-crustal deformation above the subduction system (Irsyam et al. 2017), and highlight the need to distinguish volcanic seismicity from tectonic signals.

Merapi is a stratovolcano rising to an elevation of 2,910 m above sea level (Fig. 1b) and is recognized as one of the Decade Volcanoes owing to its frequent activity, proximity to urban areas, and cultural significance (International Association of Volcanology and Chemistry of the Earth's Interior 1996). Eruptive activity in the 21st century has been characterized primarily by dome growth, lava effusion, and collapses generating pyroclastic flows, punctuated by larger eruptions in 2006 and 2010 (Surono et al. 2012). The dense surrounding population (Fig. 1b) further underscores the urgency of reliable monitoring.

At the same time, Merapi is not an unmonitored volcano. The Balai Penyelidikan dan Pengembangan Teknologi Kebencanaan Geologi (Indonesian Centre for Research and Development of Geological Disaster Technology, BPPTKG) operates a dedicated proximal monitoring network and provides a reference catalogue for volcanic and tectonic events around Merapi. This established monitoring context is important for the present study, because it allows the performance of an additional low-cost array to be evaluated against independent reference observations. Previous Merapi seismic studies have also used monitoring data to investigate pre-eruptive processes, including magma migration, stress changes, and shallow-edifice evolution (Budi-Santoso and Lesage 2016). Merapi has also been extensively investigated across multiple disciplines, including seismology (Sens-Schönfelder and Wegler 2006), petrology (Deegan et al. 2011), volcanology (Charbonnier and Gertisser 2008), deformation (Young et al. 2000), potential fields (Tiede et al. 2005), gas emissions (Allard et al. 2011), and lahars (Lavigne et al. 2000). This background supports comparison and interpretation of new observations, making Merapi a useful benchmark site for evaluating what information can still be recovered from a suboptimal monitoring configuration.

Detection and source-location methods for seismic signals conventionally rely on identifying phase arrivals, especially P- and S-waves, at individual stations (Hirata and Matsu'ura 1987; Lomax et al. 2008). Such approaches are useful for tectonic and volcanotectonic earthquakes, but they are less effective for many volcanic signals related to fluid movement, which can be small, emergent, scattered, or lacking clear phase onsets. These limitations have motivated alternative approaches that use waveform similarity, waveform coherence, or amplitude information to detect and locate volcanic signals without relying solely on arrival-time picking (Droznin et al. 2015; Journeau et al. 2022; Permana et al. 2020; Permana et al. 2022; Seydoux et al. 2016).

article in press

Another promising approach in volcano monitoring is the use of seismic arrays. A seismic array consists of multiple seismometers installed in a specific configuration at relatively short intervals. By exploiting the coherence of seismic wavefields across the array, array analysis can estimate the apparent velocity, slowness, and back-azimuth of incoming seismic waves, while also improving the signal-to-noise ratio (SNR) through stacking or beamforming (Rost and Thomas 2002). These capabilities are useful for volcanic seismicity, because volcanic tremor and other emergent volcanic signals may lack clear phase arrivals. Volcano-array studies have used frequency–wavenumber analysis, beamforming, and related methods to estimate back-azimuth and slowness, track tremor-source migration, and characterize shallow volcanic processes (Eibl et al. 2017; Hata et al. 2024). Such applications demonstrate that array processing can provide useful directional and wavefield information even when conventional phase-picking approaches are limited.

In parallel, low-cost seismic instruments have become increasingly relevant for volcano monitoring, especially where conventional broadband deployments are limited by cost, access, maintenance, safety, or logistics. Raspberry Shake instruments and related low-cost observations have been used in recent volcano-monitoring applications, such as crowdsourced acoustic observations and low-cost geophysical records of the 2022 Hunga eruption (Clive et al. 2024), a community Raspberry Shake network around Santa Ana volcano for improving seismic event detection, location, and classification (Goebel et al. 2025), and seismic-infrasound observations of eruptive activity at Yasur volcano (Reiller et al. 2026). These studies show that low-cost instruments can provide complementary observations, but their performance depends strongly on deployment geometry, distance, noise conditions, frequency content, data continuity, and validation against independent observations. Therefore, low-cost systems should be evaluated as complementary or initial monitoring tools rather than direct replacements for dedicated proximal networks.

Although array processing and low-cost seismic sensors are both increasingly used in volcano seismology, there are still limited documented evaluations of what a small, low-cost, distant array can recover under suboptimal geometry, site, distance, and resource constraints when compared against an established volcano-monitoring catalogue. This study addresses that gap by evaluating a five-station Raspberry Shake RS&BOOM array installed approximately 17 km from the summit of Merapi. The array was not designed as an optimal Merapi monitoring network, and its location introduces additional difficulties because non-volcanic signals often dominate the records and conventional phase-picking methods cannot be readily applied. Our objective was therefore to evaluate whether the array could still detect and characterize volcanic seismicity by developing a customized technique based on waveform similarity across stations and by comparing the results with the BPPTKG catalogue. The study is not

article in press

intended to replace the dedicated proximal monitoring network, but to quantify the capability and limitation of array-based volcano monitoring under constrained conditions.

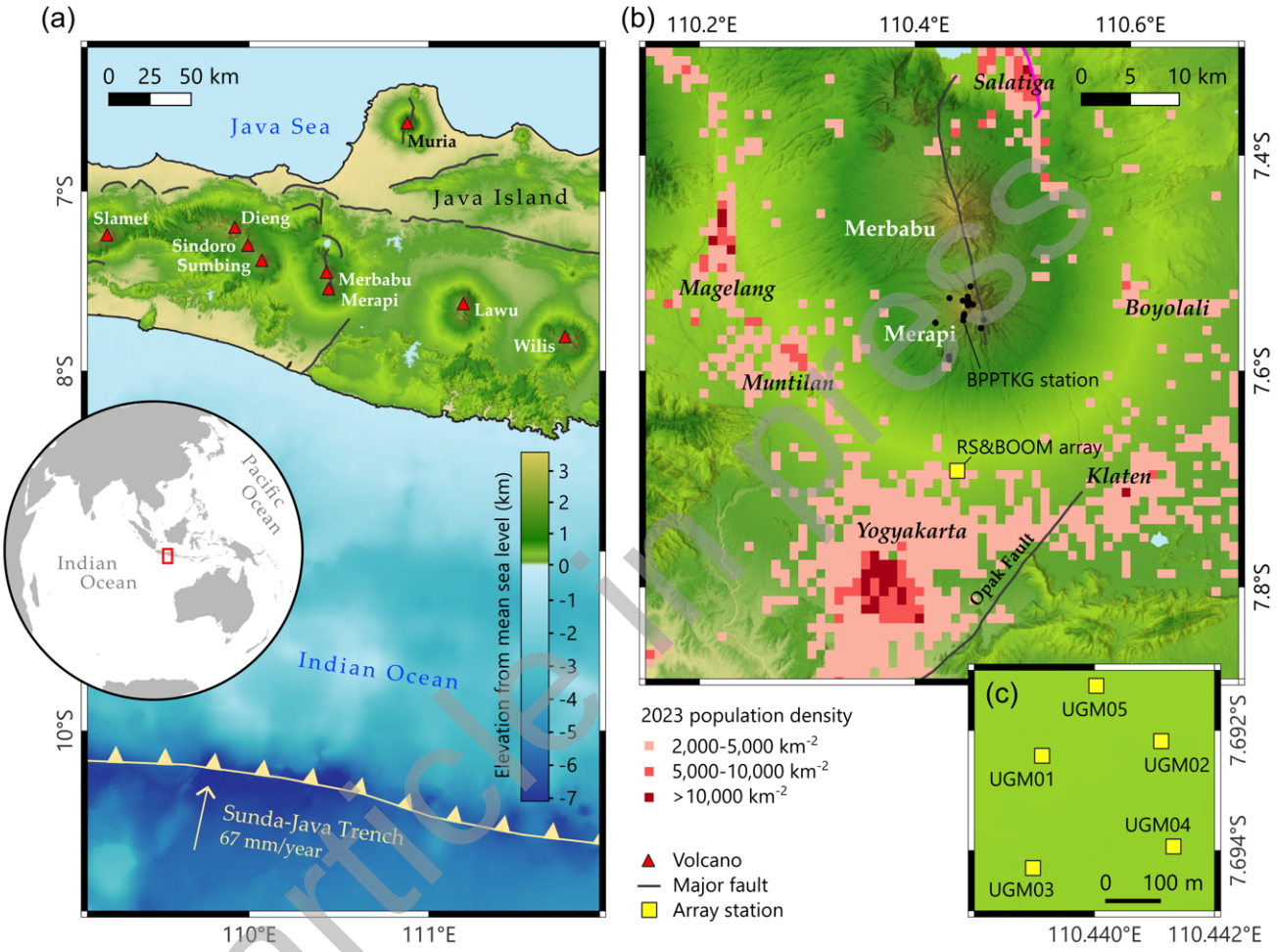


Figure 1: Overview of the study area and the RS&BOOM array. (a) Regional tectonic and volcanic setting of Central Java region, showing the Sunda-Java Trench, major crustal faults, and active volcanoes. (b) Detailed map around Merapi Volcano and its surrounding population density (>2,000 people/km^2 shown only, to avoid obscuring the topography; population density data are from Lebakula et al. 2024), highlighting the high exposure of nearby settlements. The yellow rectangle marks the array location, while black circles denote the official BPPTKG seismic monitoring stations. (c) Configuration of the array stations.

article in press

Observation data at Merapi Volcano

We investigated the performance of a seismic array installed in Ngemplak District, Sleman Regency, Yogyakarta Special Region, approximately 17 km south of Merapi's summit (Fig. 1b). The array was deployed in 2022 through a collaboration between gempa GmbH and Universitas Gadjah Mada as an early-stage experiment for array-based analyses aimed at distinguishing tectonic and volcanic seismicity. It consists of five stations arranged in a pentagonal configuration with an average interstation spacing of approximately 250 m and a maximum station separation of approximately 360 m (Fig. 1c). This configuration was selected to provide relatively balanced directional sensitivity and to reduce azimuthal bias in detecting coherent signals arriving from different directions. Each station is equipped with an RS&BOOM instrument, which records both vertical-component seismic and infrasound signals, but in this study, only recordings from the vertical-component seismic sensors were analysed. Each instrument was housed within a PVC cylinder (12 inches in diameter) mounted on a concrete base (80 cm × 80 × 30 cm) to improve ground coupling. Power was supplied from a nearby building, and continuous data streams were transmitted via mobile internet connection. Although robust in design, the array's 17-km distance from Merapi is suboptimal for volcano monitoring, as the installation was rather experimental and prioritized easy access, maintenance, and evaluation. For comparison, BPPTKG, the government agency responsible for monitoring Merapi, operates 20 dedicated seismic stations located within 6 km of the summit (Fig. 1b). Consequently, the sensitivity of our array in detecting volcanic events is expected to be lower than that of the official monitoring network.

We collected continuous daily vertical-component seismograms, stored as raw digital counts, from 27 June to 31 December 2023 (188 days) at a sampling rate of 100 Hz. Due to technical interruptions, complete five-station coverage was available only during limited intervals (16 August–7 September 2023). Nevertheless, at least three stations remained operational throughout the data period. Timing for the RS&BOOM units was provided by their internal GPS timing system. Correct time synchronization was confirmed during the initial array setup and was checked periodically during the deployment. Continuous data were streamed in SeisComP 6.7.1 software and stored daily in the proprietary raw CAPS format with limited header information, and later converted to miniSEED for analysis. All seismograms were demeaned, corrected for instrument response, and re-interpolated onto a common time grid so that samples from different stations could be compared at the same timestamps during array processing. The resulting amplitudes are expressed as vertical ground velocity.

For independent reference, we obtained the official earthquake catalogue for Merapi Volcano from BPPTKG, covering the same observation period (June–December 2023). The catalogue contains manually reviewed events

article in press

classified into volcanic, tectonic, and other or unknown types, along with key attributes such as event time, duration, amplitude, and local magnitude (M_L) estimates from the Pasarbubar station, located near the summit. The volcanic category includes low-frequency (LF), shallow volcanotectonic (VT-B), multiphase (MP), rockfall, and pyroclastic flow events (Ratdomopurbo and Poupinet 2000). Deep volcanotectonic (VT-A) category is also known, but no VT-A events were listed in the BPPTKG catalogue during our observation period, and therefore this category was not included in the subsequent comparisons. The subsurface categories of VT-B, MP, and LF represent shallow events occurring within 1.5 km beneath the summit. Following Ratdomopurbo and Poupinet (2000), VT-B events are associated with brittle rock fracturing, MP events with lava dome formation, and LF events are commonly associated with the movement of pressurized volcanic fluids. However, this interpretation is not unique, because shallow long-period seismicity may also reflect propagation-path effects, deformation, or slow rupture within weak upper-edifice materials (Bean et al. 2014). Rockfalls and pyroclastic flows, in contrast, are surface processes involving mass movement along the slopes of the volcano. This catalogue serves as a benchmark for evaluating the performance of our array, particularly in identifying volcanic earthquakes.

To further contextualize the evolution of volcanic activity at Merapi, we also extracted hourly total precipitation values from the ERA5-Land reanalysis dataset of the European Centre for Medium-Range Weather Forecasts (ECMWF) (Muñoz Sabater 2025). Daily precipitation totals were then computed at the nearest grid point located 2.33 km north of the Merapi summit.

Methods

Development of the detection method

We developed a simple seismic detection method based on a median-value approach. Vertical-component seismograms from all available stations were first combined into a single waveform by taking the median amplitudes at each time step. The envelope of this median signal was then obtained by applying a Hilbert transform and taking the absolute value of the resulting complex analytic signal.

For each time step t, we computed the median of the envelope amplitude within both a short and a long time window centred at t. The detection trace $D(t)$ was defined as the short-window median subtracted by the long-window median, conceptually similar to the STA/LTA technique (Allen 1978), but using median subtraction instead of a ratio. This formulation was chosen because median values are less sensitive to impulsive outliers,

article in press

preserve an amplitude-like scale, and allow the short-window signal level to be compared directly with the long-period background level. $D(t)$ is expressed as:

$$D(t) = \langle E(t) \rangle_{t-S/2}^{t+S/2} - \langle E(t) \rangle_{t-L/2}^{t+L/2}, \quad (1)$$

where $E(t)$ is the envelope of the median signal, and $\langle E(t) \rangle$ denotes the median amplitude of E within a time window of length specified by S (for the short window) and L (for the long window) each centred at t.

The repeated use of median calculations helps suppress incoherent amplitudes and emphasize coherent seismic signals. Taking the median across all array seismograms reduces noise contributions that are not consistently observed at every station. Coherent signals from Merapi or tectonic sources are expected to arrive nearly simultaneously across the array, since the interstation spacing is small compared to the seismic wavelengths of interest. This assumption holds for frequencies below 10 Hz, where most volcanic and tectonic seismicity occurs (Permana et al. 2022; Ratdomopurbo and Poupinet 2000).

Applying a short-window median filter to the envelope further removes spurious or anomalous amplitudes while preserving only coherent signals, effectively smoothing the median envelope $E(t)$. This windowing scheme is conceptually similar to the conventional STA/LTA method, in which sudden amplitude increases are identified relative to the background level. Prior to detection, the seismograms were bandpass filtered to emphasize the dominant energy of volcanic and tectonic events while suppressing long-period and high-frequency noise. Because the optimal band depends on the noise and signal characteristics of our suboptimal array site, the selected band was determined from the empirical examination of observed seismicity described in "Characteristics of observed seismicity" section.

A seismic detection was defined when the detection trace $D(t)$ exceeded a specified trigger threshold. Each instance of this condition is referred to as a “detection,” and the time interval during which $D(t)$ remained above the threshold is defined as the detection duration. In practice, a detection does not always correspond to a single earthquake, as false triggers or rapid multiple detections of the same event may occur. To mitigate these cases, we excluded detections shorter than a specified minimum duration and merged detections separated by less than 4 s, since the amplitudes of an earthquake may temporarily fluctuate below and above the trigger, artificially terminating a detection before immediately initiating a secondary one for the same event. The short- and long-window lengths, trigger threshold, and minimum detection duration were likewise selected from the empirical examination of observed seismicity described in "Characteristics of observed seismicity" section.

article in press

For subsequent analyses, we extracted seismogram segments using the start and end times of each detection. When the detection duration exceeded 60 s, an additional 60 s of data were appended before and after the detection duration. For shorter detections, the pre- and post-detection extensions were set equal to the detection duration. This procedure ensured that the extracted waveforms included both the primary signal and sufficient background noise for comparison.

In addition to identifying seismic detections, our approach also extracted a set of parameters for each detection. These parameters were used to characterize the detected signals and to distinguish events of volcanic origin. The description of these characterization parameters is presented in the following sections.

Beampacking analysis

We applied beampacking analysis, the time-domain equivalent of frequency–wavenumber analysis, to estimate the apparent velocity and back-azimuth of seismic waves recorded by the array. This method assumes a plane-wave front propagating across the array and computes interstation delay times by testing a range of trial slowness vectors (Rost and Thomas 2002; Schweitzer et al. 2012). For a given horizontal slowness vector $\boldsymbol{u}_{hor}$, the array beam is expressed as:

$$B(t) = \frac{1}{M}\sum_{i=1}^{M} x_i\,(t + \boldsymbol{r}_i \cdot \boldsymbol{u}_{hor}), \qquad (2)$$

where M is the number of array stations, $x_i(t)$ is the seismogram recorded at station i, and $\boldsymbol{r}_i$ is the location vector of station i relative to the array centre. The optimum apparent velocity and back-azimuth are obtained from Equation 2 by searching for the slowness vector that maximizes the beam power.

The analysis was performed using a sliding window with a specified length and time shift. The chosen window length ensured that several wave cycles were included while maintaining sufficient temporal resolution. Prior to beampacking, the seismograms were interpolated to an experimental sampling rate of 10,000 Hz. This oversampling was applied solely for computational convenience, providing a finer grid for delay-time alignment without introducing any new spectral information beyond that of the original recordings. In addition, the oversampling procedure proved useful for the elevation-based parameter described in the following section. The effective resolution of the slowness estimates remains fundamentally constrained by the signal frequency content and the approximately 360 m aperture of the array.

article in press

For each detection, the back-azimuth was derived from the optimum horizontal slowness vector that maximized the beam power (Rost and Thomas 2002). To quantify the reliability of these estimates, we computed the circular standard deviation (referred to simply as the standard deviation hereafter) of back-azimuth values within the first half of the detection duration, using it as a measure of uncertainty. This interval was selected because the initial portions of the waveforms are expected to contain the most reliable direct arrivals, whereas the later portions are more likely to be affected by scattering. Following the same assumption, the apparent velocity was computed from the optimum horizontal slowness, and the values were averaged over the first half of the detection duration.

To facilitate interpretation, back-azimuths were expressed relative to north, with negative values indicating directions west of north and positive values indicating directions east of north. This convention helps distinguish events originating from Merapi, as the volcano lies to the north of the array. We also transformed the back-azimuth values into weights that quantify directional consistency of each detection relative to Merapi. We assigned a weight of 1 for back-azimuths between -3.29° and 5.95°, 0 for back-azimuths between 12.83° and -11.40°, and linearly interpolated the weight between these ranges (see Fig. S1 in the Supplementary Material). The weights were then averaged over the first half of the detection duration and used, together with the mean apparent velocity and the standard deviation of back-azimuth values, to characterize the detections.

article in press

Elevation-based characterization parameter

Another characterization approach was developed to account for differences in arrival times across the array stations by assuming a hypothetical source beneath Merapi. This method was adapted from the source location determination scheme proposed by Permana et al. (2020). However, due to the limited aperture, poor azimuthal coverage, and suboptimal distance of our array, reliable location estimates were not feasible. Instead, we modified the approach to derive a characterization parameter that evaluates the consistency of observed signals with assumed source elevations beneath the volcano. This modification shifts the focus from precise event location to relative characterization of detections.

Rather than aligning seismograms by applying slowness-based time shifts, as is common in array analyses, we computed theoretical travel times for a range of assumed source elevations beneath Merapi summit (precisely beneath 7.5412°S, 110.4456°E). For each elevation z, we defined a measure of signal coherence at time t as:

$$C(z,t) = \left|\frac{1}{M}\sum_{i=1}^{M} x_i\,(t + \tau_i(z) - \tau')\right|, \quad (3)$$

where $\tau_i(z)$ is the theoretical travel time from elevation z to station i, and τ' is the mean travel time across all stations. The value of $C(z,t)$ thus quantifies the degree of waveform coherence when the signals are time-shifted according to a hypothetical source elevation.

The theoretical travel times $\tau_i(z)$ were estimated using the pseudobending ray-tracing technique (Um and Thurber 1987). This procedure requires a subsurface velocity model, which we constructed independently, as no widely accepted velocity model for Merapi currently exists. We developed a one-dimensional model with smoothly varying velocities spanning elevations from -5 km to 2.9 km relative to mean sea level (Fig. S1). For the shallowest 500 m, we adopted the generic volcanic velocity profile (Lesage et al. 2018), while deeper layers were represented by a linear velocity gradient from a reference profile for Central Java (Koulakov et al. 2007) and the CRUST 1.0 model (Laske et al. 2013) at the nearest grid point, located approximately 8 km northeast of Merapi.

Although this simplified 1-D model cannot capture Merapi's known structural heterogeneity, it provides a practical basis for consistent travel-time estimation within our characterization framework. We used S-wave velocities, as S-waves are typically dominant and associated with the largest amplitudes of volcanic earthquakes (e.g., Permana and Aoyama 2023). This 1-D model was then extended into a simplified 3-D representation for ray tracing by assuming no lateral velocity variation. Topography was not explicitly included, as all estimated ray paths remained beneath the surface and did not intersect the terrain. To improve computational efficiency, we precomputed all ray paths for a range of source elevations beneath Merapi's summit and used these precomputed paths to obtain the theoretical travel times required in Equation 3.

We demonstrated that sufficient differences exist in the theoretical travel times between stations to yield meaningful values of $C(z,t)$, even considering the small aperture of the array relative to the distance to Merapi (Fig. S1). These differences are on the order of less than 0.01 s, which is another reason we oversampled the seismograms beforehand. Oversampling enables fine temporal shifting of the seismograms, resulting in a higher elevation resolution of the $C(z,t)$.

We applied the elevation-based parameter computation to each time window defined for the beampacking procedure. For each window, $C(z,t)$ was computed over a range of assumed source elevations, and the elevation z at which C reached its maximum was taken as the optimum value. The elevation-based parameter was defined as this optimum elevation, which should not be interpreted as the true source depth of the event, given the high uncertainty associated with our limited array configuration. Instead, it serves as a relative indicator reflecting the consistency of the observed signals with volcanic or non-volcanic origins. Because shallow events beneath Merapi and more distant tectonic events are expected to differ in their relative arrival-time patterns across the array, their

article in press

signals may yield distinct ranges of optimum elevations. This parameter was therefore introduced as an empirical measure of whether a detection is more consistent with a shallow Merapi-related source or with a more distant tectonic source. We then averaged the elevation-based parameter over the first half of the detection duration to obtain a consistent measure of detection characterization.

Results

Characteristics of observed seismicity

An example of unfiltered seismograms recorded on 29 August 2023 (Fig. 2a) illustrates the strong influence of local seismic noise. Elevated and irregular amplitudes dominated the records from 22:00 to 15:00 UTC (05:00 to 22:00 local time), but these fluctuations were not correlated among stations and are therefore attributed to anthropogenic activity near the array site. In contrast, nighttime recordings exhibited lower amplitudes, consistent with reduced human activity. This pronounced diurnal noise pattern reflects the suburban environment of the array, located approximately 10 km north of Yogyakarta City (Fig. 1b).

To better distinguish the different types of signals, we transformed the seismograms into the frequency domain and computed the median spectrogram across all stations (Fig. 2b). Using median values emphasizes coherent amplitudes shared among stations while suppressing local disturbances, thereby providing a clearer representation of array-wide signals. The median spectrogram revealed that anthropogenic noise dominated frequencies above 2 Hz, with daytime enhancements and a brief relative quiescence around midday (05:00–06:00 UTC or 12:00–13:00 local time) consistent with typical working hours of human activity. Persistent energy below 0.8 Hz was attributed to microseisms (Friedrich et al. 1998; Hasselmann 1963).

Identifying volcanic seismicity is challenging with our array configuration, as these typically small-magnitude events are easily masked by anthropogenic and microseismic noise. In contrast, a relatively quiet frequency band between 0.8 Hz and 1.8 Hz displayed intermittent short-duration bursts of energy. Volcanic seismic events, associated with the movement of volcanic fluids, are commonly observed over a broader frequency range of 0.5–10 Hz (Nishimura and Iguchi 2011; Permana et al. 2022; Ratdomopurbo and Poupinet 2000), within which our narrow band is embedded. The 0.8–1.8 Hz band was therefore selected for subsequent analyses, as it effectively suppresses both anthropogenic and microseismic noise while preserving the most likely volcanic signals.

Filtering the seismograms within this band (Fig. 2c) increased the SNR and improved the visibility of coherent transient signals, while computing the median envelope across stations (Fig. 2d) further enhanced signal clarity.

article in press

Peaks in the median envelope correspond to potential seismic events, highlighted by their coherence across the array.

Manual inspection of the BPPTKG official catalogue confirmed that several peaks in the median envelope on 29 August 2023 (Fig. 2d) correspond to catalogued VT-B earthquakes and rockfall events, demonstrating the array's potential to detect genuine volcanic signals. A high-energy burst at 04:40 UTC, with its spectral peak within the microseism band, was confirmed as a tectonic M_w 5.8 earthquake that occurred in the Banda Sea at 04:34 UTC at a depth of 220 km, according to the catalogue of the Indonesian Agency for Meteorology, Climatology, and Geophysics (BMKG). This observation further validates the array's capability to capture distant, large-magnitude events that are typically dominate at lower frequencies (Permana et al. 2023).

Based on this empirical examination of the recorded seismicity, we selected the processing parameters used for the full analysis. We performed beampacking analysis using a 3 s sliding window shifted every 1 s. Detection traces $D(t)$ were then computed using short- and long-window lengths of 20 s and 600 s, respectively. Within the 0.8–1.8 Hz band, anthropogenic noise was largely suppressed, although its long-term effects remained visible in the spectrograms. The 600 s window was designed to capture this long-term variability, which was subsequently subtracted from the short window. A trigger value of 0.03 μm/s was defined, which was sufficient to capture the peaks.

The minimum detection duration was set to 15 s to ensure sufficient data for reliable estimation of apparent velocity, back-azimuth, and the elevation-based parameter. To enhance computational efficiency for rapid detection, $D(t)$ was computed at 1 s increments and interpolated back to the original 100 Hz sampling rate.

article in press

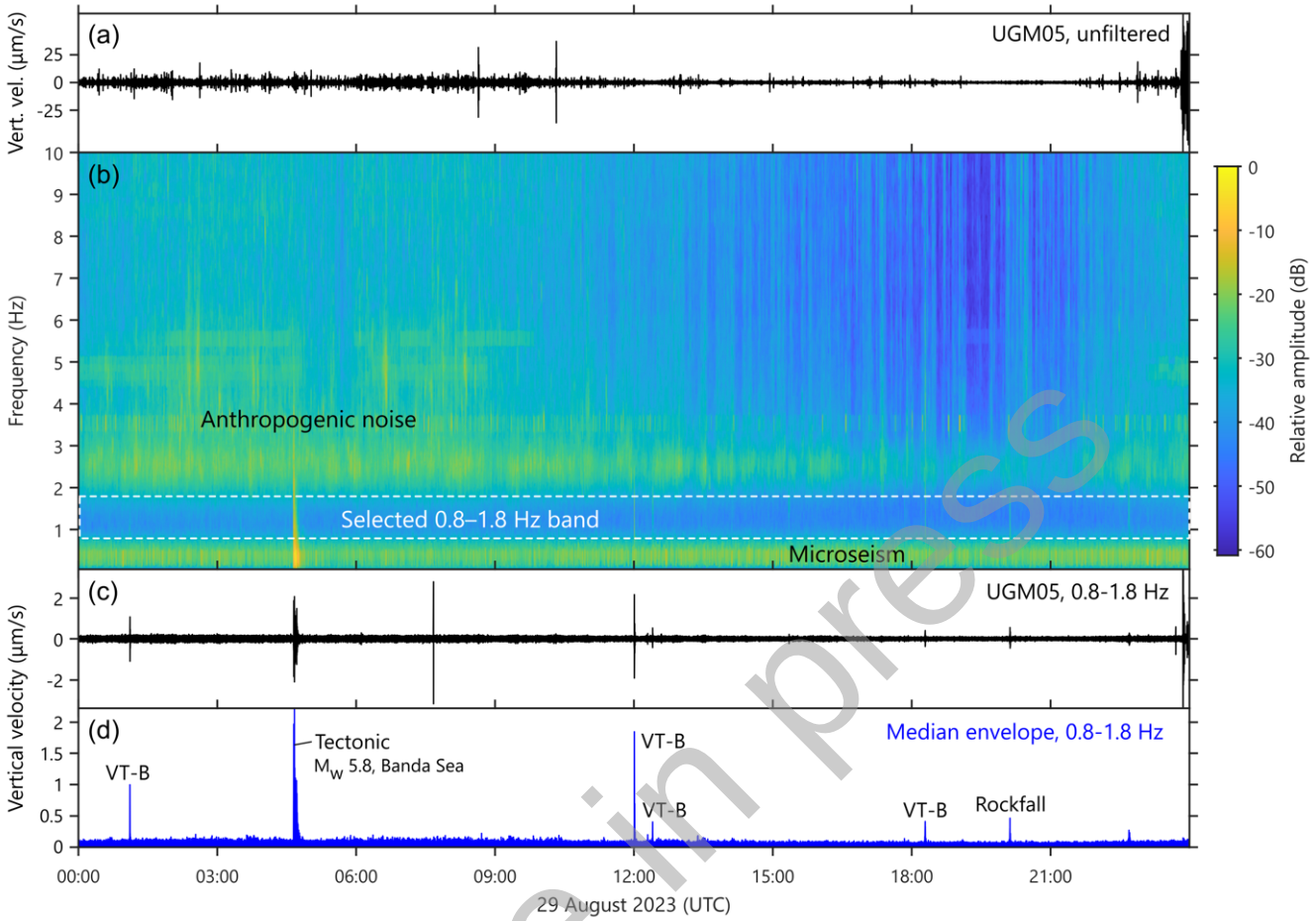


Figure 2: Example of one-day seismogram examination on 29 August 2023. (a) Unfiltered vertical velocity seismogram from station UGM05. (b) Median spectrogram computed from vertical-component records across all available stations; the white dashed rectangle indicates the selected 0.8–1.8 Hz bandpass used in subsequent analyses. (c) UGM05 seismogram filtered at 0.8–1.8 Hz. (d) Median envelope of the array. Peaks correspond to seismic events manually confirmed in the BPPTKG catalogue, with tectonic earthquake parameters confirmed using the BMKG catalogue.

article in press

Application of detection and characterization methods

We applied the detection and characterization methods, using parameters determined from the examination of observed seismicity, to continuous recordings between 27 June and 31 December 2023. As representative examples, we present one event from each of the categories listed in the official BPPTKG catalogue during this period: tectonic and VT-B events in Fig. 3; rockfall and MP events in Fig. 4; and pyroclastic flow and LF events

in Fig. 5. The M_w 5.8 tectonic earthquake and a VT-B event, corresponding to the highest peaks in the median envelope shown in Fig. 2, are included here for reference. The other volcanic categories are each represented by their largest-M_L event. Comparing these different types of events is particularly useful for evaluating whether the detection and characterization behaviour agrees with our assumptions and formulation, especially within the selected narrow frequency band of 0.8–1.8 Hz.

The median spectrograms of the event examples further show how the selected frequency band represents different portions of each signal. These spectrograms were computed from vertical-component records at all available stations and summarized using the median spectral amplitude at each time-frequency sample. The tectonic and VT-B examples both contained coherent energy over a relatively broad frequency range (Figs. 3a and 3i). However, the tectonic example was dominated by lower frequencies than the selected 0.8–1.8 Hz band, whereas the VT-B example showed clearer energy within this band. This indicates that, for tectonic events, our filtering may not capture the main spectral content of the recorded signal, which may contribute to the less stable back-azimuth estimates described below. In contrast, the volcanic examples in Figs. 4–5 were generally distinguishable only up to approximately 3 Hz, above which the signals were increasingly affected by the high-frequency noise already shown in Fig. 2b.

Our median-based detection successfully captured the essential part of the seismic signals within each detection duration, as shown by the filtered seismograms, median envelopes, and detection traces. The strategy to avoid triggering multiple detections of the same event was also effective, as demonstrated toward the end of the tectonic detection (Figs. 3b–d), where the detection trace $D(t)$ fluctuated around the trigger level. For short events lasting less than five minutes, subtracting the 600 s long-window median from the short-window median effectively removes the background noise level, thereby improving the trigger accuracy in capturing the start and end of the events (Figs. 3j–l, 4b–d, 4j–l, 5b–d, and 5j–l).

We also compared the performance of our median-based detection with the conventional STA/LTA approach (Figs. 3d, 3l). The STA/LTA method was applied to the absolute seismogram from station UGM05, consistent with standard single-station implementations. Using identical short- and long-window lengths, the STA/LTA trace exhibited a comparable shape to $D(t)$, and with an appropriate trigger threshold, it could yield similar detection start and end times. Therefore, the median-based detection should not be interpreted as universally superior to STA/LTA. In this study, however, median subtraction was preferred because it follows the same array-coherence logic used throughout the analysis, is less affected by incoherent amplitudes across stations, and keeps the detection trace more directly comparable to event amplitude levels than the STA/LTA ratio.

article in press

Beampacking analysis confirmed distinct differences between the tectonic and VT-B examples (Fig. 3). Apparent velocities were generally higher for the tectonic earthquake, while the VT-B event exhibited lower apparent velocities, consistent with its shallower source (Figs. 3e, 3m). Apparent velocity tended to be highest during the early arrivals, interpreted as faster phases such as P-waves. The tectonic example also showed greater uncertainty in the back-azimuth, reflecting the limited directional resolution of our small-aperture array when applied to distant or complex sources (Fig. 3f). In contrast, the VT-B example showed more stable values toward the possible Merapi direction during the first half of the detection duration, supporting our preference to summarize the characterization parameters within this interval and thereby avoid later values influenced by scattered waves (Fig. 3n). Their weights and elevation-based parameter values demonstrated the expected contrast between tectonic and shallow Merapi-related events, where higher values are expected for arrivals from Merapi (Figs. 3g–h and 3o–p). For the elevation-based parameter, ray paths from greater depths correspond to lower values, whereas shallower sources beneath Merapi or at the surface are represented by higher values (Figs. 3h, 3p).

The rockfall and MP examples (Fig. 4) revealed more complex characterization behaviour. Their apparent velocities, back-azimuths, and weights (Figs. 4e–g and 4m–o) are consistent with volcanic detections, as demonstrated by the VT-B example. Both examples displayed stable high elevation-based parameter values, reflecting their surface or shallow origins (Figs. 4h, 4p). In the MP example, the apparent-velocity estimate did not show the initial higher-velocity phase observed in the VT-B example. Instead, a higher apparent-velocity estimate appeared near the end of the detection, possibly reflecting another event that occurred shortly afterwards (Figs. 4j, 4m). The close temporal spacing of these successive events, combined with the typically emergent onsets of MP events (e.g., Ratdomopurbo and Poupinet 2000), highlights the trade-off between our 15 s minimum detection duration and the sensitivity to rapid succession of events. Under such conditions, the detection may fail to register later events or may combine multiple events into a single detection.

The pyroclastic flow and LF examples (Fig. 5) further illustrate the limitations of using a single narrow frequency band. The pyroclastic flow example showed apparent velocities, back-azimuths, and elevation-based parameter values consistent with volcanic detections (Figs. 5e–f, 5h), but variations in the back-azimuths were more difficult to capture using our weighting scheme (Fig. 5g). In contrast, the LF example exhibited characteristics differing from the other volcanic types, but only during the early part of the signals within the first half of the detection duration (Figs. 5m–p). Despite showing higher apparent velocity compared to other volcanic types, this does not necessarily indicate a deeper source, particularly because long-period seismicity can be strongly affected by propagation-path effects and weak shallow materials (Bean et al. 2014). This interpretation is also consistent with the description of Merapi seismicity by Ratdomopurbo and Poupinet (2000), who placed LF sources within a

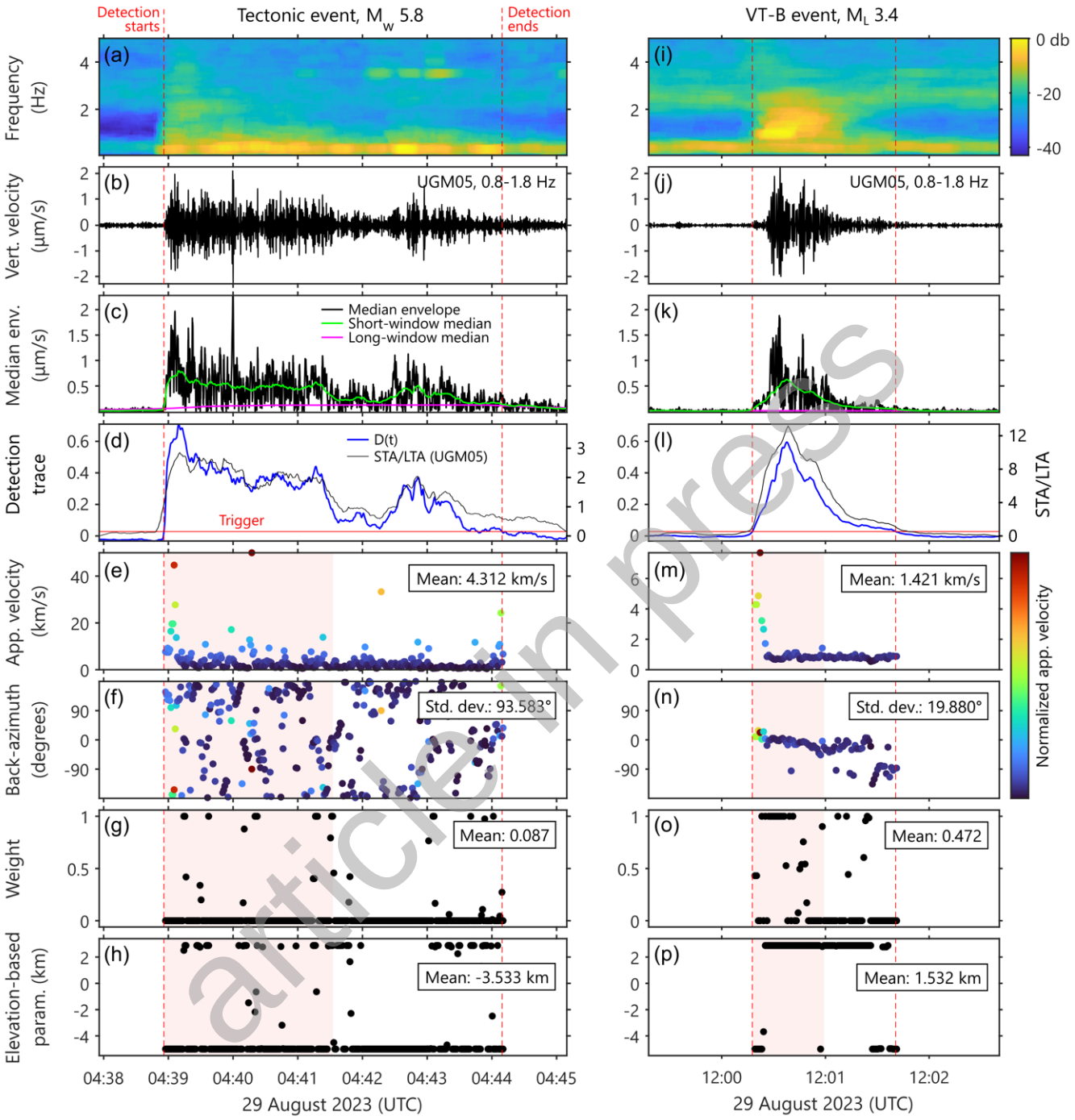
article in press

shallow zone beneath the summit. Thus, the elevated apparent velocity of our LF event likely reflects additional factors beyond source depth alone and requires further investigation.

The event spectrograms also clarify several limitations of the filtered detections. For the rockfall and pyroclastic-flow examples, energy above 1.8 Hz appeared to continue after the lower-frequency signal used in our detection (Figs. 4a and 5a), suggesting that the 0.8–1.8 Hz band may miss later higher-frequency signal components from surface processes. For the MP example, the spectrogram supports the interpretation that the earliest part of the signal was not fully captured by the detection window (Fig. 4i), possibly excluding the part with the highest apparent velocities. The later high apparent-velocity estimate near the end of the MP detection did not show the same spectral signature as the main MP signal, so its event type cannot be confirmed from this example alone. The LF example, meanwhile, showed an impulsive signal more similar to the VT-B example than to the longer-duration surface events (Fig. 5i).

The consistency between our detection and characterization results and the known or inferred physical processes of the corresponding event types, despite some extent of discrepancies, suggests that the narrow 0.8–1.8 Hz band retains useful information representative of each event category. This finding supports the suitability of the selected band for extended application across our entire seismic recordings.

article in press

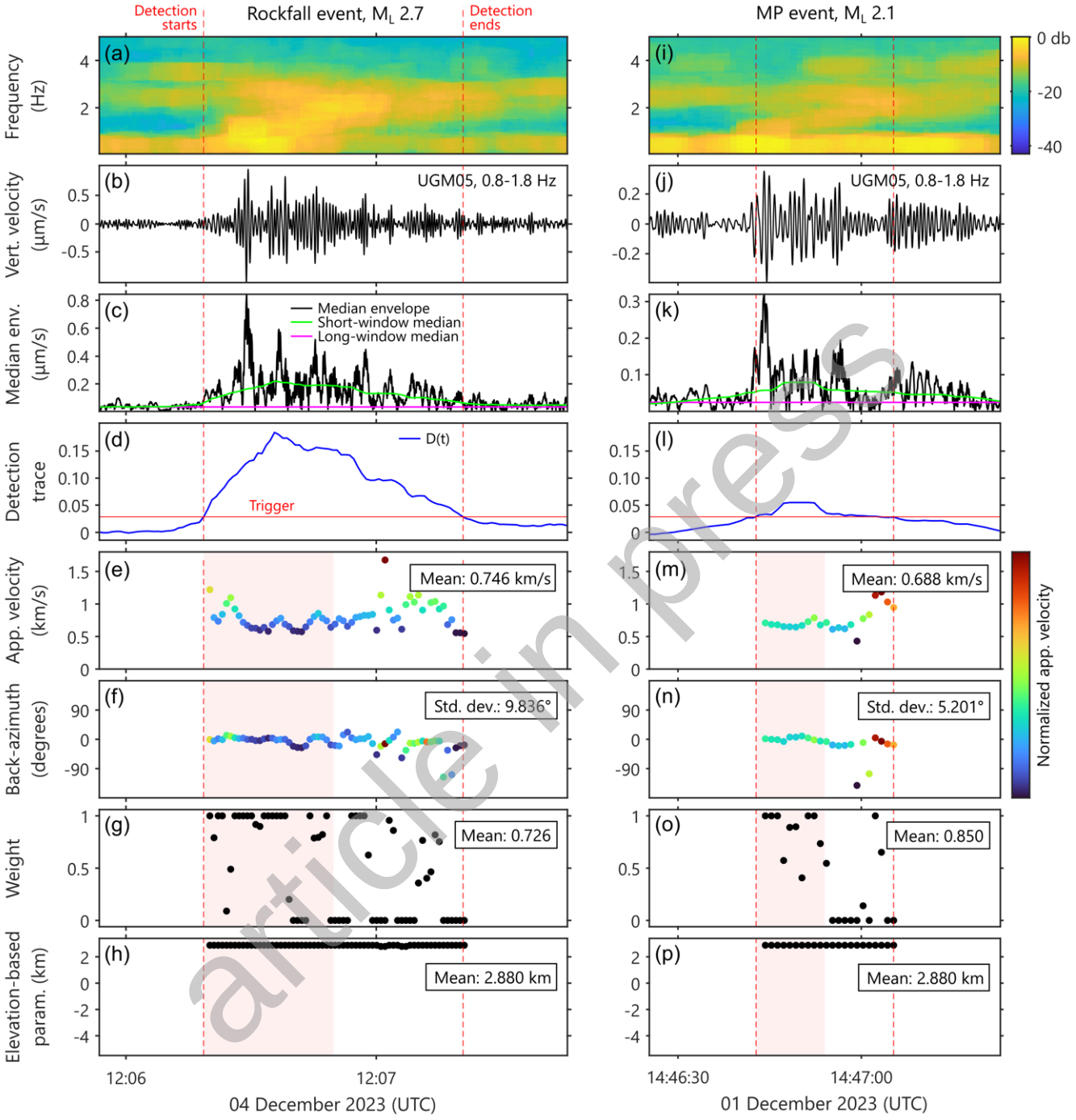


article in press

Figure 3: Example of detection and characterization of a M_w 5.8 tectonic event (left panels) and a VT-B event (right panels). (a, i) Median spectrogram computed from vertical-component records across all available stations. (b, j) Filtered vertical-velocity seismograms from UGM05 station. (c, k) Median envelopes and median values computed using shifting short and long windows. (d, l) Detection traces showing the start and end of a detection, during which

the trace exceeds the trigger. STA/LTA traces computed using the same shifting windows are shown for comparison. (e, m) Apparent velocity. (f, n) Back-azimuth. (g, o) Weights derived from the back-azimuths. (h, p) Elevation-based characterization parameter. Red-shaded areas denote the first half of the detection duration, over which the mean or standard deviation of characterization parameters are calculated.

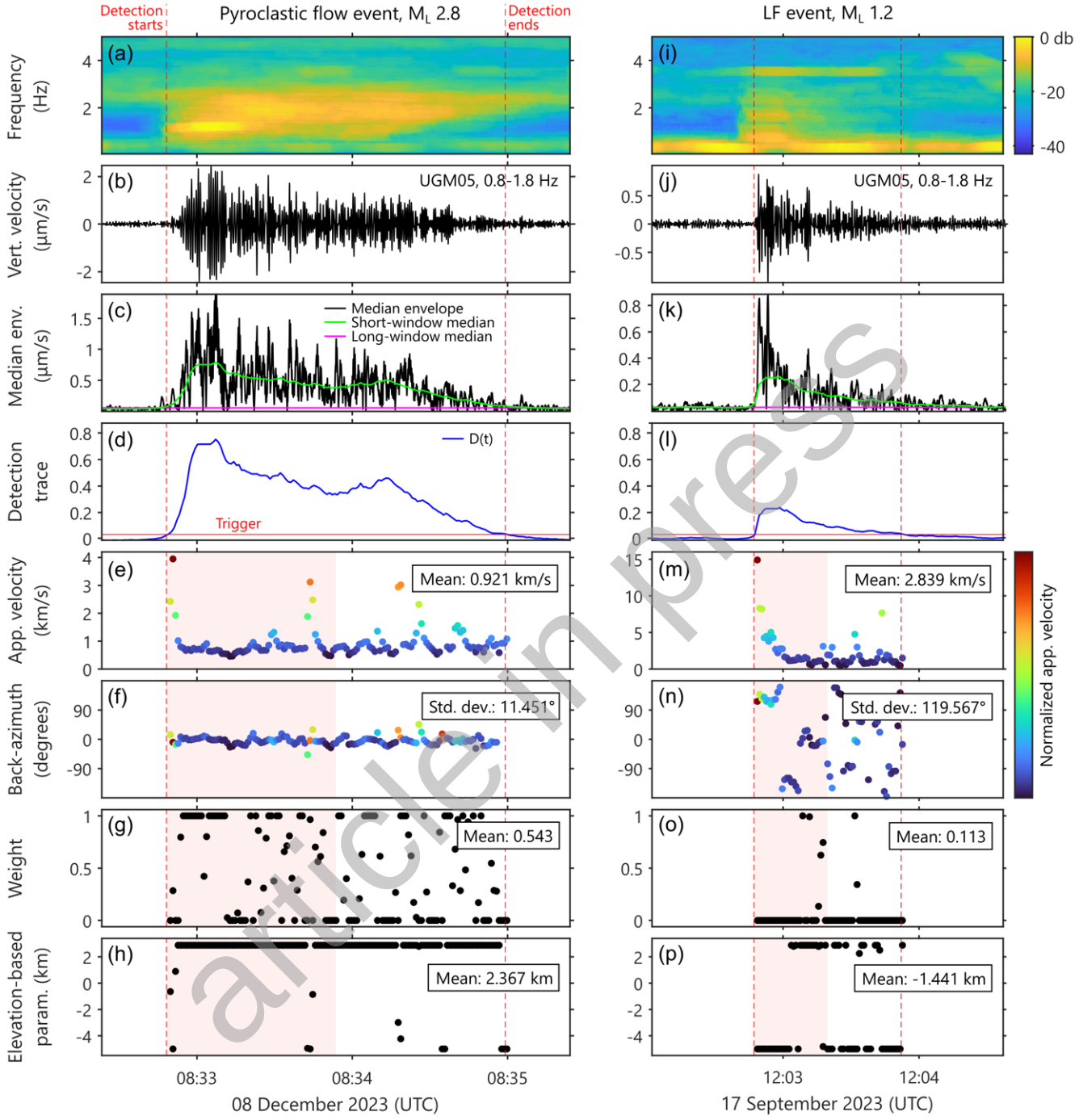
article in press



article in press

Figure 4: Example of detection and characterization of a rockfall event (left panels) and an MP event (right panels). Panel descriptions are identical to those in Fig. 3.

460



article in press

Figure 5: Example of detection and characterization of a pyroclastic flow event (left panels) and an LF event (right panels). Panel descriptions are identical to those in Fig. 3.

Examination of detection performance

Comparison with reference catalogue

Applying our detection method to seismic recordings between 27 June and 31 December 2023 yielded 1,677 detections with at least three available stations, which were retained for further analysis. To objectively evaluate which detections corresponded to real seismic events, we matched our detections with the BPPTKG catalogue. Because our detection times represent arrivals at the array, whereas the BPPTKG catalogue reports event origin times, different matching assumptions were applied to volcanic and tectonic events. For volcanic events from Merapi, ray-tracing results indicate that signals should arrive at the array approximately 10 s after the origin time. We therefore considered a volcanic catalogue event to be matched when a detection occurred within 20 s after its origin time. For tectonic events, the timing relationship is less direct. These events may originate outside the Merapi volcanic system and arrive from various azimuths, so the signal can reach our array before, after, or nearly simultaneously with the stations used in the Merapi monitoring catalogue. Moreover, the BPPTKG catalogue is primarily designed for Merapi monitoring, and tectonic events are used here mainly as non-volcanic reference events rather than as regional earthquake locations optimized for precise origin-time comparison with our array. We therefore allowed a broader matching window from 10 s before to 20 s after the catalogue time for tectonic events. Using these criteria, 637 detections were matched with catalogued events, representing 37.98% of all detections and 1.07% of 59,663 events listed in the BPPTKG catalogue. The remaining 1,036 detections (61.78%) were not matched with the BPPTKG catalogue and were treated as unclassified detections.

Daily comparisons between the number of matched events show that our detection captured significantly fewer volcanic events than the catalogued ones, as expected from our suboptimal array setup (Figs. 6a–f). We also compared the BPPTKG catalogue duration and local magnitude M_L for volcanic events to identify the ranges that could be confidently detected by our array (Fig. 7). The matched detections comprised 214 VT-B events, 103 MP events, 1 LF event, 91 rockfall events, 5 pyroclastic flow events, and 223 tectonic events. However, the success rates varied greatly across event types: 23.86% for VT-B, 0.30% for MP, 0.90% for LF, 0.38% for rockfall, 27.78% for pyroclastic flow, and 80.80% for tectonic events.

The temporal evolution of subsurface volcanic events in the BPPTKG catalogue (VT-B, MP, and LF) shows a peak of seismic unrest around early July, followed by renewed activity increase around early August that culminated in early December (Figs. 6a, 6c, and 6e). VT-B and LF occurrences then decreased around early October, while MP event counts remained high until the early-December peak. Surface-related events also reflected these activity peaks (Figs. 6b, 6d), with more pyroclastic-flow events occurring around early December. Meanwhile, rockfall

article in press

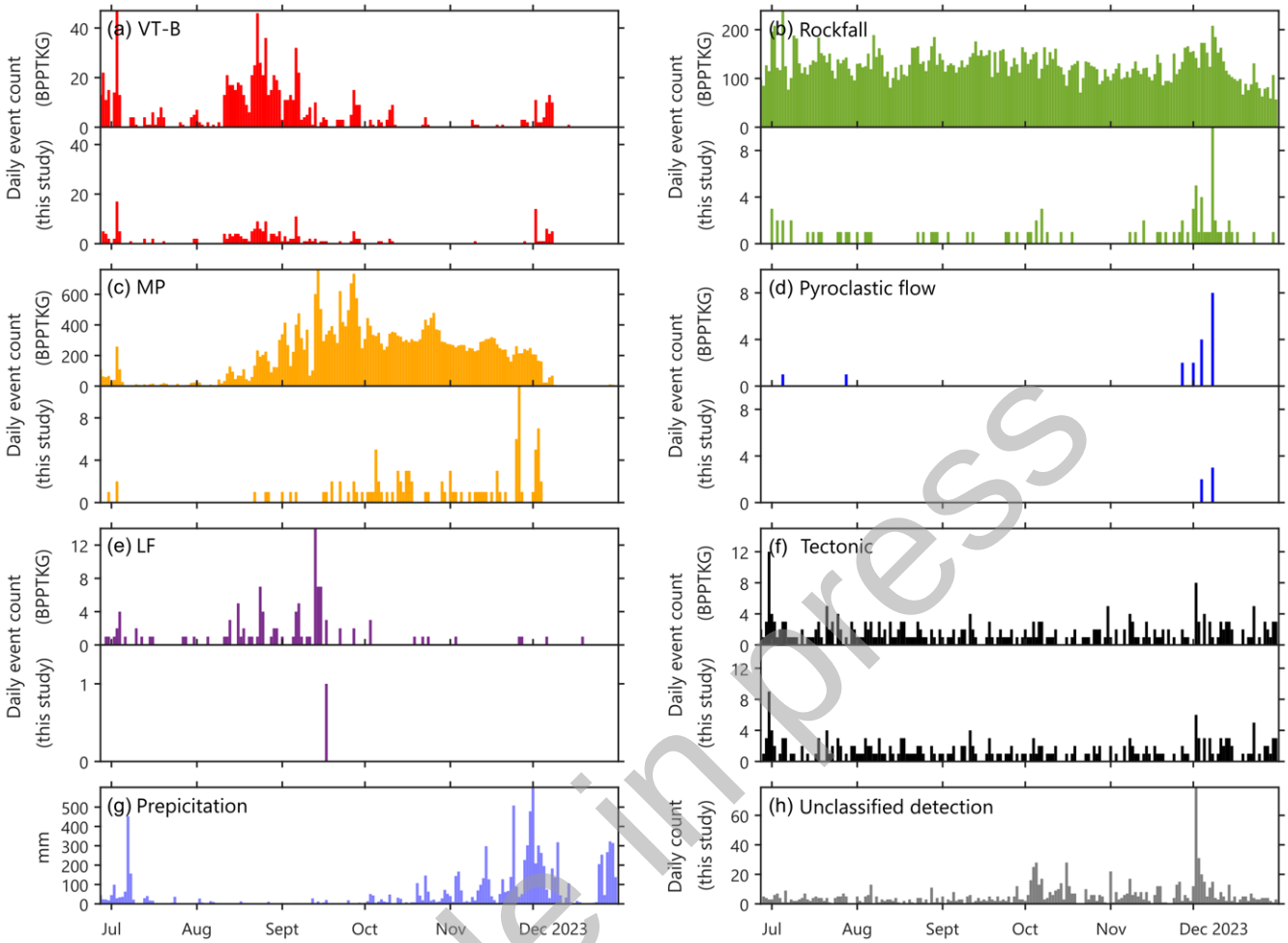
events remained frequent during our observation period, with increased counts around early July and early December, followed by a distinct decrease after the later peak. Despite the array's reduced sensitivity, the matched detections still highlight the early-July and early-December unrest peaks for most volcanic event categories, except for LF. In contrast, the matched tectonic detections are more consistent with those officially reported, showing two prominent peaks in late June and early December (Fig. 6f).

The magnitude and duration distributions in Fig. 7 further show the differences among volcanic event types and the subset detected by our array. Tectonic events were excluded from the magnitude–duration comparison because the official monitoring network does not routinely determine accurate parameters for tectonic earthquakes. Our matched VT-B detections generally correspond to catalogue events with M_L>1.5, with the detection tendency most evident for events of approximately M_L>2.0 (Fig. 7a) and durations around 10 s or longer (Fig. 7b). MP events generally have M_L<2, but both their magnitude and duration increased from mid-September to early December, during which more MP events were detected by the array. LF events have magnitudes similar to MP events, and the MP and LF categories have durations comparable to VT-B events, consistent with their relatively impulsive character. Rockfall events have magnitudes similar to MP and LF events but tend to have longer durations, reaching approximately 200 s. Several rockfall events were detected throughout the data period, with more detected events in early December. Pyroclastic flows are generally more intense than rockfall events, showing higher magnitudes and longer durations.

The rainfall data provide additional temporal context for the daily seismicity comparison (Fig. 6g). Rainfall episodes occurred in early July and from early October onward, with higher rainfall intensity toward late November and early December. These rainfall data were used only as contextual information for the interpretation of volcanic activity in the Discussion section.

The remaining detections not matched with events in the BPPTKG catalogue, referred to as "unclassified" detections, remained relatively stable before October, averaging 2.39 per day, but increased thereafter with a pronounced peak in early December (Fig. 6h). Some proportion of false detections is expected given the simplicity of our detection approach; however, the timing of these peaks, which roughly coincides with periods of heightened volcanic activity, should be interpreted with caution. Considering the location of the array, signals from environmental or anthropogenic origin which potentially, though not necessarily, related to the volcanic unrest, may also be present within this category.

article in press



525 **Figure 6: Daily distribution of official datasets and detection results in this study during 27 June–31 December 2023. Comparison between the BPPTKG catalogue and the matched detections is shown for (a) VT-B, (b) rockfall, (c) MP, (d) pyroclastic flow, (e) LF, and (f) tectonic events. (g) Daily total rainfall from the ERA5-Land dataset at a grid point near the Merapi summit. (h) Unclassified detections that have no corresponding match in the BPPTKG catalogue.**

article in press

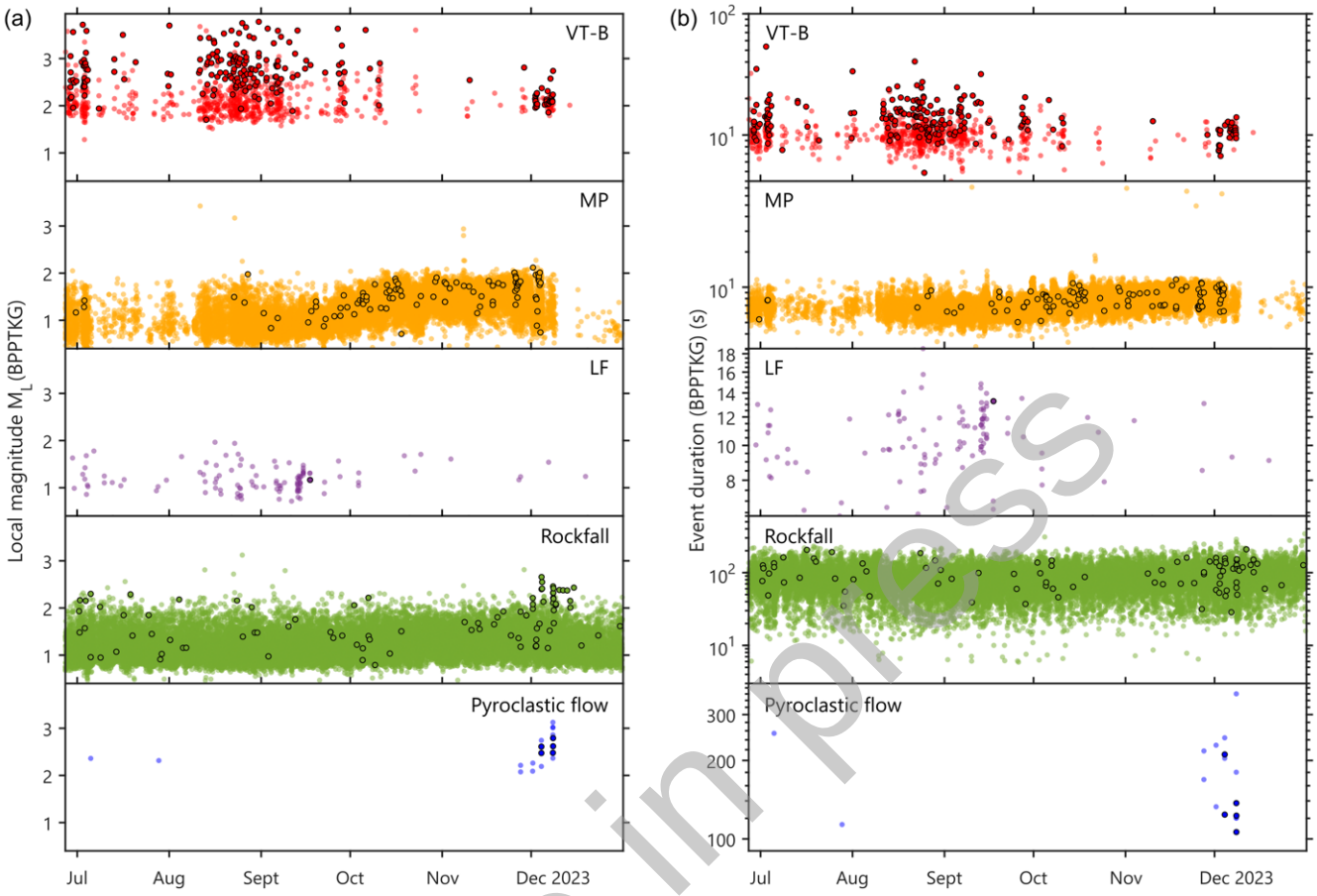


Figure 7: Temporal distribution of volcanic events (VT-B, MP, LF, rockfall, and pyroclastic flow) from the BPPTKG catalogue. Comparison is provided in terms of (a) estimated local magnitude M_L and (b) event duration. Events that are also detected in this study are marked by black circles.

article in press

Magnitude comparison and duration sensitivity

We used the maximum of the short-window median $\langle E(t)\rangle_{t-S/2}^{t+S/2}$ in Equation 1, referred to hereafter as $\max\langle E\rangle_S$, as a proxy for event strength. We then compared the logarithm of this quantity with the estimated M_L from the BPPTKG catalogue for volcanic events (Fig. 8a). For VT-B events, the comparison showed an approximately linear relationship. We fitted this relationship empirically to the observed $\log(\max\langle E\rangle_S)$ and M_L pairs and obtained the following expression:

$$M_L = 0.36\log(\max\langle E\rangle_S) + 3.23, \qquad (4)$$

with an R^2 value of 0.59. This relationship should be interpreted as a VT-B-specific empirical trend within our array configuration. MP and rockfall events do not show similarly linear relationships, while the relationships for LF and pyroclastic flow events remain inconclusive because only a small number of matched detections were available for these categories.

Comparison between our detection durations and the corresponding event durations from the BPPTKG catalogue revealed different proportionality for each event category, including tectonic ones (Fig. 8b). VT-B, MP, and tectonic events showed clearer proportional relationships than the other categories. For events originating from Merapi (VT-B, MP, and LF), small variations in event duration corresponded to greater variations in the detection duration. For tectonic events, the comparison between catalogue duration and detection duration was more directly proportional, although considerable scatter remains. Duration comparison for rockfall events indicates that our array has lower sensitivity to variations in rockfall duration. Pyroclastic flow events also showed extended and variable durations that were less directly comparable with the more impulsive volcanic or tectonic sources.

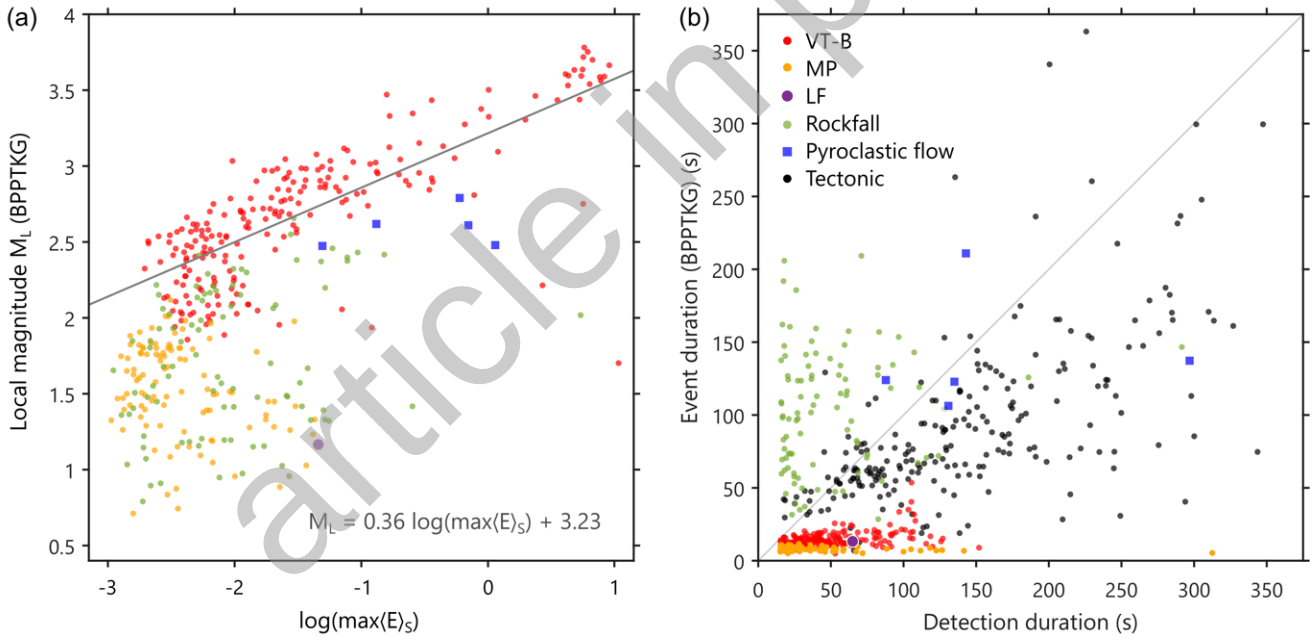


Figure 8: Comparison of magnitude and duration of matched detections. (a) Logarithm of maximum short-window median $\max\langle E\rangle_S$, representing the event strength, compared with the estimated M_L from the BPPTKG catalogue. The grey line denotes the fitted empirical relationship for VT-B events (equation shown). (b) Comparison between detection duration and event duration from the BPPTKG catalogue. The grey line illustrates the ideal linear relationship.

article in press

Performance of the characterization

We first examined the overall distribution of characterization values to evaluate their consistency with the BPPTKG catalogue. The comparison indicated that tectonic and VT-B detections occupy more distinct regions of the parameter space, whereas MP, LF, rockfall, and unclassified detections overlap more strongly. Because these relationships are more clearly interpreted through their dependence on signal strength, detection duration, and signal shape, the following sections examine the characterization values together with amplitude and waveform information.

Comparison of characterization values with amplitudes

The characterization parameters, including the detection duration, were compared against the corresponding $\log(\max\langle E\rangle_S)$ to examine whether their variations or the reliability depended on event strength, using $\max\langle E\rangle_S$ as a proxy for magnitude (Fig. 9). The comparison revealed differing relationships among parameters. The values associated with MP, LF, and rockfall events were the most difficult to distinguish from one another or to consistently identify as volcanic, compared with VT-B and tectonic-related values within a similar $\log(\max\langle E\rangle_S)$ range.

We observed a relatively weak positive relationship between $\log(\max\langle E\rangle_S)$ and mean apparent velocity (Fig. 9a), as well as between $\log(\max\langle E\rangle_S)$ and the standard deviation of back-azimuth (Fig. 9b). Higher-magnitude events were generally associated with higher apparent velocities and larger uncertainty in the back-azimuth estimates. Detection duration itself showed a stronger dependence on event magnitude, appearing nearly linear for VT-B events when compared with the logarithm of the $\max\langle E\rangle_S$ (Fig. 9c). This linear trend for VT-B can be empirically approximated as:

$$\log(\max\langle E\rangle_S) = 0.034\,\Delta t_d - 3.083, \qquad (5)$$

where Δt_d denotes the detection duration. This empirical relationship has an R^2 value of 0.92. By substituting Equation 5 into Equation 4, we obtained an alternative empirical expression for estimating M_L directly from the detection duration, optimized for VT-B events:

article in press

$$M_L = 0.012\,\Delta t_d + 2.115. \qquad (6)$$

Equation 6 provides a simplified duration-based estimate for VT-B events within this dataset only. Equations 4–6 are therefore empirical, site-specific, frequency-band-specific, and configuration-specific relationships. They should not be transferred to other instruments, sites, frequency bands, or array geometries without recalibration.

Comparisons between $\log(\max\langle E\rangle_S)$ and the mean elevation-based parameter (Fig. 9d) or mean weight (Fig. 9e) did not reveal any clear relationships. Nevertheless, we observed that higher-magnitude VT-B events tended to be associated with lower weights. Meanwhile, pyroclastic flow events displayed patterns generally consistent with those of VT-B events, except for their notably longer duration. The parameter comparison also indicated that unclassified detections shared magnitudes, detection durations, and characteristic values similar to those of most MP and rockfall events (Fig. 9). This similarity indicates that some unclassified detections may have volcanic characteristics, although their origin remains uncertain because no corresponding events were found in the BPPTKG catalogue. It is therefore possible that some of these detections originated from non-volcanic sources.

Tectonic detections generally occupied the higher-apparent-velocity and higher-back-azimuth-uncertainty ranges, consistent with the event examples in Fig. 3 and with their more distant or complex source paths (Figs. 9a–b). Compared with VT-B events, tectonic detections showed a weaker and more scattered relationship between detection duration and $\log(\max\langle E\rangle_S)$, indicating that duration is less directly related to event strength for tectonic signals in our array records (Fig. 9c). Comparisons between $\log(\max\langle E\rangle_S)$ and the mean elevation-based parameter (Fig. 9d) or mean weight (Fig. 9e) did not reveal clear amplitude-dependent relationships. However, these panels still show a clear separation between tectonic and VT-B detections: tectonic events cluster at lower elevation-based parameter and weight values, whereas VT-B events cluster at higher values. This indicates that the elevation-based parameter and weight are more useful as source-consistency discriminators than as amplitude-dependent quantities.

article in press

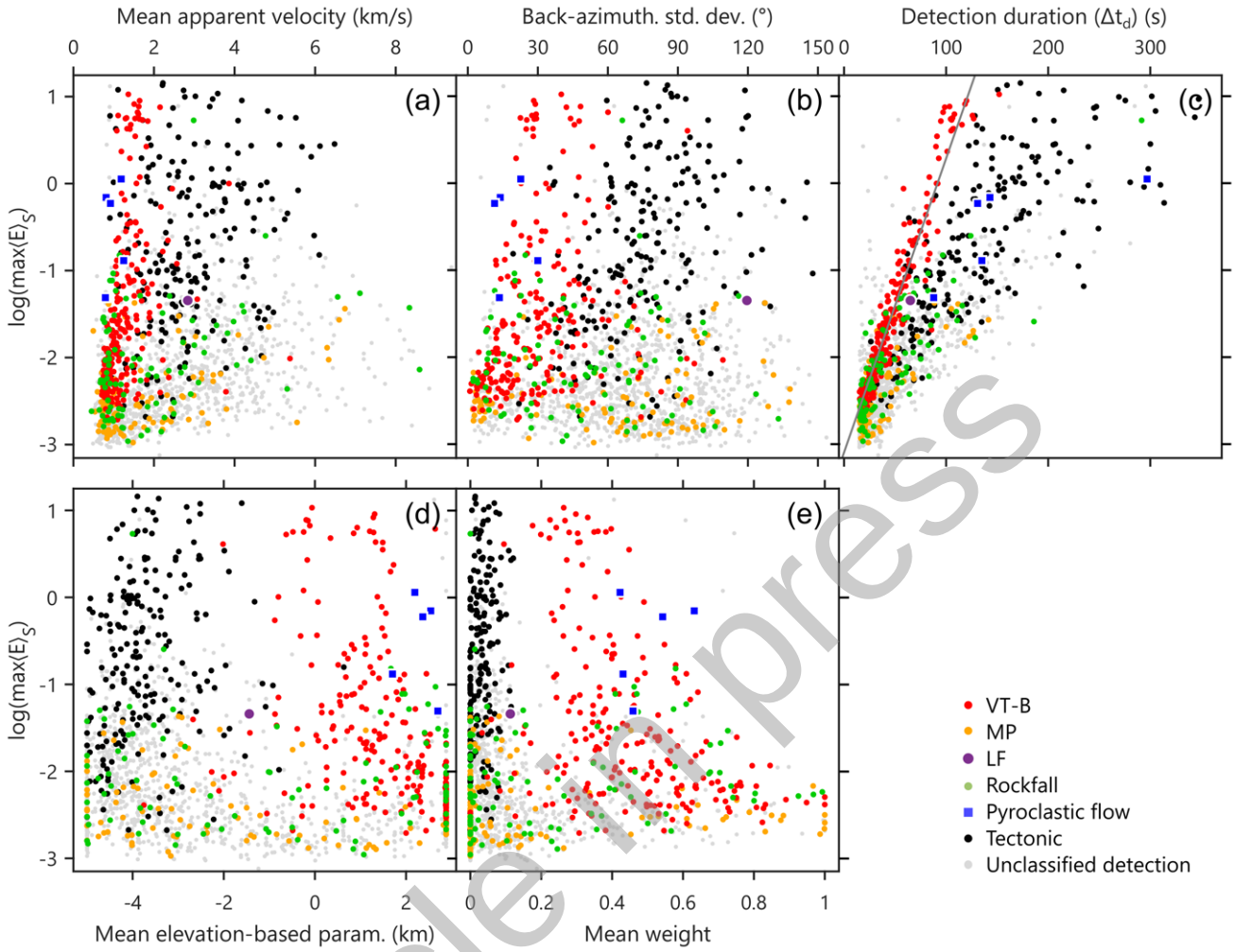


Figure 9: Comparison of $\log(\max\langle E\rangle_S)$, used as a proxy for event magnitude, with characterization parameters and detection duration. Comparisons are shown against (a) mean apparent velocity, (b) standard deviation of back-azimuth, (c) detection duration, (d) mean elevation-based parameter, and (e) mean weight. The grey line in (c) shows the best-fitting VT-B relationship, $\log(\max\langle E\rangle_S) = 0.034\,\Delta t_d - 3.083$.

article in press

Signal characteristics within the detection duration

While the detection and characterization examples demonstrated characteristic values that help distinguish volcanic events from tectonic ones (Figs. 3–5), applying the same approach to all seismic recordings revealed that these distinctions did not consistently hold for all detections. So far, we have examined how the summarized characterization values over the first half of the detection duration vary with event amplitude (a proxy for

magnitude) and with detection duration itself. However, the variability and uncertainty in these relationships may also reflect differences in the internal consistency of the detected signals. To assess this, we compared the short-window median traces during the detection duration for event category (Fig. 10). These traces were normalized, plotted, and vertically offset according to $\max\langle E\rangle_S$, allowing us to examine how signal shapes vary with both magnitude and detection duration.

The comparison showed that the detected signal shapes were most consistent for the VT-B category (Fig. 10a), displaying an approximately linear increase in detection duration with increasing signal peak $\max\langle E\rangle_S$, as summarized in Fig. 9c. We also observed several inconsistencies, including two VT-B events that were mistakenly merged into a single detection, and two others that triggered prematurely. In contrast, MP and rockfall events exhibited greater fluctuations in amplitude, reflecting higher waveform complexity that may explain the difficulty in classifying them as volcanic events. Similar complexity likely also occurs in LF events, though this could not be fully examined here due to their limited number (Figs. 10b–d).

Pyroclastic flow events exhibited signal shapes and durations that were largely independent of event magnitude, reflecting their complex generation mechanisms involving moving or multiple sources interacting with the ground surface. We observed both single- and multi-peaked signals, with peak amplitudes not necessarily occurring during the early portion of the waveform. It should be noted that $\max\langle E\rangle_S$ is not directly proportional to the estimated M_L in the BPPTKG catalogue. This is evident from the signal with the largest $\max\langle E\rangle_S$ in Fig. 10e, which differs from the event with the largest M_L shown in Fig. 5, consistent with the comparison in Fig. 8a.

In contrast, tectonic events displayed distinct signal characteristics within the detection duration (Fig. 10f). Two general waveform types were identified, both exhibiting more complex amplitude variations than the VT-B events. The first type consists of signals with a single, well-defined peak during their early part, while the second type shows irregular amplitude fluctuations with multiple peaks, although the strongest peak often still occurs near the beginning of the signal. Determining the source processes responsible for these signal types is challenging within our narrow 0.8–1.8 Hz band, since the observed waveforms depend on several factors: event distance and depth relative to the array, magnitude, and the relative contributions of body and surface waves, all of which are only partially captured within this frequency range. It is also possible that the second signal type was affected by noise or non-tectonic contamination, obscuring the genuine tectonic signal.

Overall, our detection of tectonic events indicated that detection duration is only weakly proportional to the event magnitude. This finding highlights the importance of ensuring that the detection duration covers a sufficient amount of signal information, ideally emphasizing the direct energy from the source, which is best represented within the first half of the detection duration.

article in press

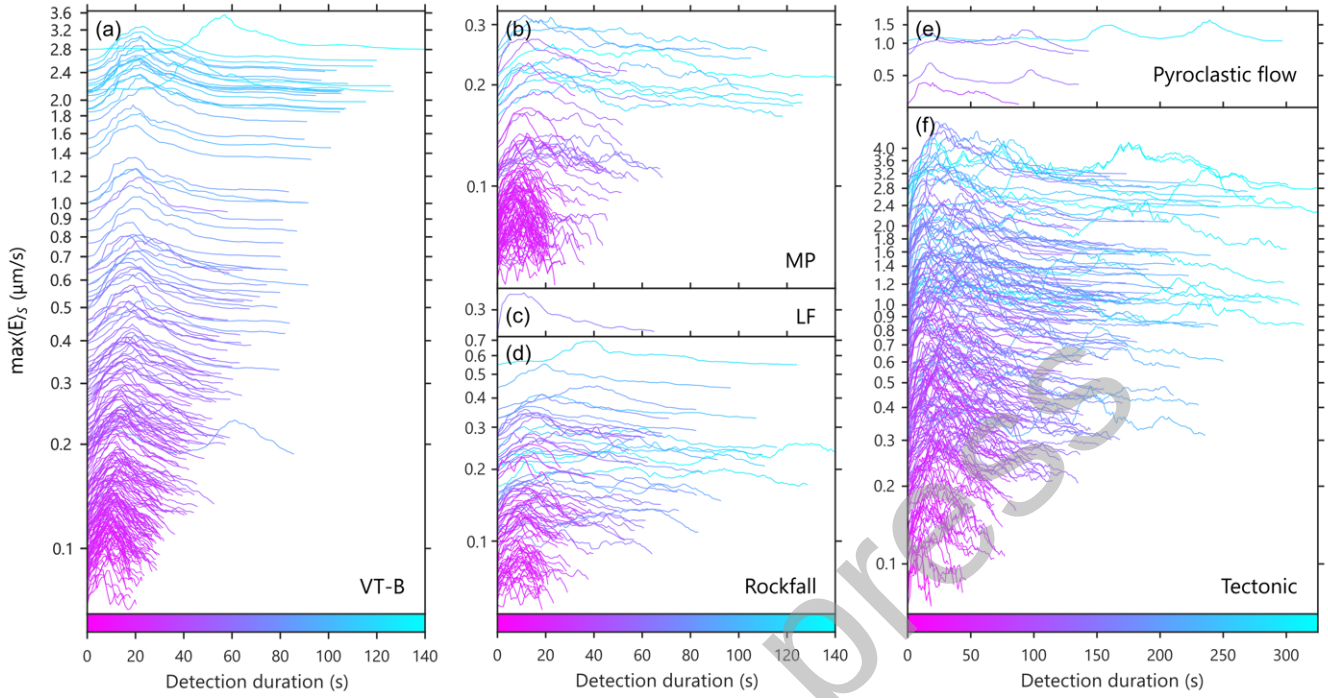


Figure 10: Comparison of normalized short-window medians representing the signal shape during the detection duration, shown for each matched event category: (a) VT-B, (b) MP, (c) LF, (d) rockfall, (e) pyroclastic flow, and (f) tectonic. Traces are vertically offset according to their respective $\max\langle E\rangle_S$ values, and line colors indicate the detection duration of each trace. Note that the y-axis labels are in logarithmic scale.

article in press

Computational stability from signal oversampling

Oversampling the seismograms to higher sampling rates was essential for our array configuration, as it enabled finer time-shifting of the signals to account for interstation arrival-time differences smaller than the original sampling time of 0.01 s. Without oversampling, such small delays would limit the precision of detailed event characterization, particularly for signals originating from Merapi, when using the beampacking and elevation-based parameter analyses. This procedure should be interpreted as a numerical interpolation step, rather than as an improvement of the original timing accuracy. Possible timing drift or residual synchronization errors would therefore remain a source of uncertainty in the array-based delay-time estimates.

We demonstrated the improvement in characterization stability gained from finer signal alignment by experimenting with our VT-B event example in Fig. 3. Three 3-s signal segments were defined (Fig. 11a): one

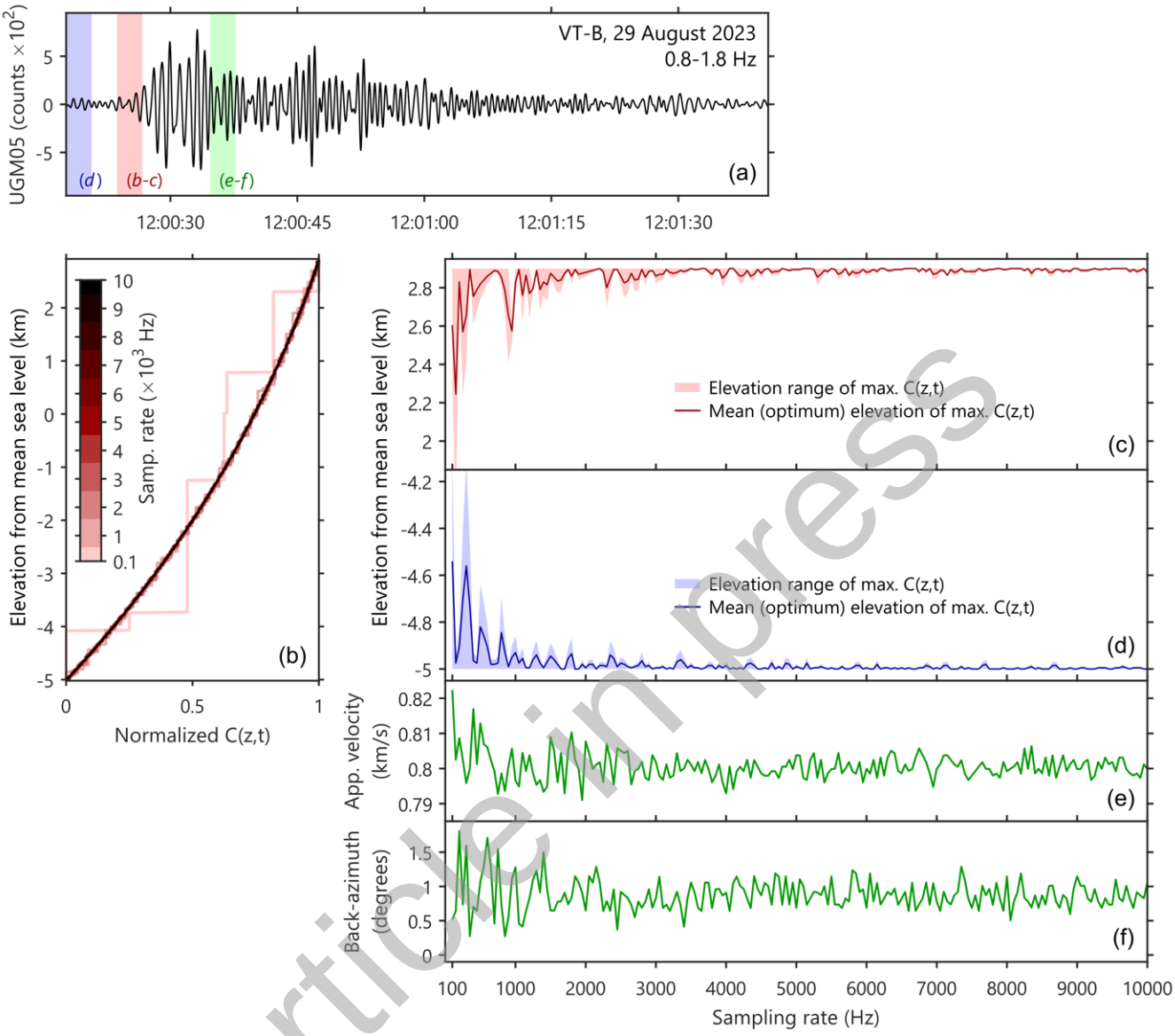
corresponding to a deep assumed source elevation of -5 km relative to mean sea level, another representing a shallow assumed source elevation of 2.9 km, approximately the elevation of Merapi summit, and a third in which the back-azimuth was closest to the direction of Merapi summit. We recalculated $C(z,t)$ for the first two segments and the apparent velocity and back-azimuth for the third segment using various sampling rates, ranging from the original 100 Hz up to 10,000 Hz, with increments of 50 Hz.

Fig. 11b illustrates the principle of the elevation-based parameter, which involves computing $C(z,t)$ at various assumed source elevations, defined relative to mean sea level beneath Merapi summit, and identifying the optimum elevation where $C(z,t)$ is maximized. This optimum elevation is the elevation-based parameter and should be interpreted as a relative characterization value rather than a true source elevation or depth. When the sampling rate is too low, the maximum $C(z,t)$ tends to occur over a broader elevation range rather than at a single, well-defined optimum. Increasing the sampling rate narrows this range, producing a smoother $C(z,t)$ curve with respect to elevation by adding details only possible from finer time-shifting of the seismograms. This improvement in the details of $C(z,t)$ occurs at all source elevations, as demonstrated in our experiments for both shallow and deep assumed sources (Figs. 11c–d). In our computations, the optimum elevation was obtained by averaging the elevations at which maximum $C(z,t)$ occurred. occurred. The variability in these values was greater at lower sampling rates.

A similar improvement with increasing sampling rate was also observed for apparent velocity and back-azimuth estimates. However, despite the reduction in variability, stable convergence was not fully achieved even at a 10,000 Hz sampling rate (Figs. 11e–f). For sampling rates between approximately 3,000 Hz and 10,000 Hz, apparent velocity varied within 0.01 km/s of the mean (Fig. 11e), while back-azimuth varied within 0.5 degrees (Fig. 11f). This residual instability likely reflects the limited resolving capability of our small-aperture array in accurately determining the optimum slowness.

It is important to note that the stability of these parameters directly influences all derived characterization values. These computations using various higher sampling rates also provide a basis for evaluating the minimum sampling rate necessary when lower computational loads are required. The desired level of stability is inherently qualitative and may vary depending on the analysis objectives. In this study, we adopted a 10,000 Hz sampling rate as an idealized choice to achieve the highest possible stability within our computational constraints. For more practical applications where computational efficiency and processing speed are prioritized, and some trade-off with stability is acceptable, a lower sampling rate could be employed, depending on the array configuration.

article in press



article in press

Figure 11: Oversampling experiment using the VT-B event on 29 August 2023. (a) Filtered seismogram from UGM05 station. The red- and blue-shaded intervals denote the time windows used to compute the elevation-based parameter $C(z,t)$ in (b)–(d), while the green-shaded interval marks the segment used for beampacking analysis in (e)–(f). (b) $C(z,t)$ values as a function of assumed source elevation relative to mean sea level beneath Merapi summit, computed at the original sampling rate (100 Hz) and several higher rates with a 1,000 Hz increments. (c) Optimum elevations, corresponding to the elevation-based parameter, and their uncertainty ranges (shaded area) at various sampling rates for the shallow estimated elevation case. (d) Optimum elevations and their uncertainty ranges for the deep estimated elevation case. (e) Apparent velocities. (f) Back-azimuths.

Effect of station availability

We simulated scenarios in which data from one or more array stations were unavailable. This situation occurred frequently during our observation period (87.77% of the analysed days) and was likely caused by hardware or electronic failures, interruptions in data transmission, or environmental conditions. Because the affected stations could not be predicted in advance, this experiment also served to assess how irregular changes in the number and configuration of available stations might affect the array's accuracy and sensitivity in determining the back-azimuth of volcanic events.

We selected 94 matched VT-B events with complete five-station coverage. The VT-B category was chosen because these events exhibit a relatively clear and consistent characteristic pattern when observed with our array. For each possible combination of three, four, and five stations, we recalculated the back-azimuths for all 94 events using the same parameter settings as in the beampacking analysis, focusing only on the first half of the detection duration. The circular mean and standard deviation of the back-azimuth values were then averaged within three magnitude ranges: M_L 1.8–2.5, M_L 2.6–2.9, and M_L 3.0–3.7. We limited this comparison to the back-azimuth parameter, as it is generally more stable than the apparent velocity and elevation-based parameter, both of which may vary substantially during the earliest parts of the events. The results of these simulations are provided in Fig. S2 in the Supplementary Material.

In terms of the summarized back-azimuth results, the lowest standard deviations of less than 27° were obtained when using all five stations. With four stations, the standard deviation remained below 43°, whereas three stations produced variations of up to 88°. Larger-magnitude events tended to show higher standard deviations, consistent with the relationship observed in Fig. 9b. The mean back-azimuths also exhibited increasing westward shifts with magnitude, with values -3.60°, -6.10°, and -8.41° for the three magnitude ranges, respectively. Consequently, during the back-azimuth weighting, larger-magnitude events tended to yield lower weights, explaining the observed trend in the mean weights shown in Fig. 9e. When only three stations were available, both the mean and standard deviation of back-azimuth values became less stable and displayed greater variability. The largest standard deviation was obtained when stations UGM01 and UGM02 were excluded. However, similarly large values were also obtained when excluding UGM02 and UGM03, or UGM04 and UGM05. When four stations were used, omitting UGM02 consistently increased the standard deviation. Across these varying station configurations, no predictable pattern emerged that could suggest an optimal subset of stations when full array coverage was unavailable. The factors governing the variability of back-azimuth values under different station combinations

article in press

remain unclear, but likely involve site effects and path effects between Merapi's actual seismic sources and individual stations, both further compounded by the geometric limitations of our array setup.

Discussion

Detection capability and frequency-band limitations

The comparison with the BPPTKG catalogue shows that our array captured only a small fraction of the official volcanic catalogue but performed comparatively well for tectonic and VT-B events (Fig. 6). This discrepancy can be partly attributed to differences in event magnitude and duration (Fig. 7), the large source–array distance, the SNR at the array site, and the limited portion of seismic energy represented within our narrow 0.8–1.8 Hz band.

Accurate seismic detection conventionally relies on the frequency band most representative of the event type, event magnitude, source–station distance, and SNR. Our narrow 0.8–1.8 Hz band minimized noise contamination but introduced a trade-off: it may not fully represent the spectral characteristics of all event categories. The current volcanic event classification follows Ratdomopurbo and Poupinet (2000), who showed that VT-B and MP events have broad frequency content up to 8 Hz, LF events are dominant below 3 Hz, and rockfalls typically exhibit durations 2–4 times longer than VT or MP events. These, however, are generalized characteristics rather than guaranteed ones. This trade-off is also visible in the event-example spectrograms in Figs. 3–5, where the selected band captures a useful but incomplete part of the recorded signals, especially for tectonic and surface-process events.

Tectonic earthquakes, while generally dominant at lower frequencies, possess a broader spectral content that can still be captured within the 0.8–1.8 Hz band. This likely explains their relatively high detection success. Some exceptions exist, for instance, weak teleseismic or distant surface-wave arrivals (e.g., Permana et al. 2023), but typical tectonic events in our region occur at greater distances than the Merapi–array distance. Consequently, the recorded signals are similar between our array and the official monitoring network, resulting in the higher success rate for tectonic detections.

The influence of event duration on detection performance is further constrained by our windowing strategy. The detection traces may inadvertently merge overlapping or closely spaced events, while the imposed 15 s minimum detection duration may cause shorter and smaller events to be missed. Although this constraint is necessary to suppress false detections, it also reduces the sensitivity of our method to short-duration signals. These limitations

article in press

are particularly relevant for MP, LF, and rockfall events, which were rarely matched despite being abundant in the BPPTKG catalogue.

Interpretation of amplitude and duration relationships

The information on event magnitude and duration is represented differently in our detections because of the narrow frequency band and the array's distance from Merapi. Naturally, seismic signals recorded at increasing distances are more strongly affected by scattering due to medium heterogeneity, path effects, site effects, and instrument response. Seismic amplitudes also attenuate with distance through both geometrical spreading and intrinsic absorption within the medium (e.g., Battaglia and Aki 2003).

The empirical expression relating $\max\langle E\rangle_S$ to M_L provided an approximate linear fit for VT-B events, but the same relationship did not clearly apply to the other volcanic event categories (Fig. 8a). This likely reflects the combined effects of the limited 0.8–1.8 Hz band, source complexity, path effects, site effects, and the suboptimal array geometry. The relationship should therefore be regarded as empirical and specific to this array configuration, rather than as a transferable magnitude relation.

The duration comparison also reflects differences in source process and propagation effects. Theoretically, event durations should appear longer at greater distances due to the increasing influence of scattered and surface waves. This behaviour was evident for VT-B, MP, and tectonic events, all of which can be regarded as having relatively impulsive, point-like sources with clearer energy-scaling characteristics that govern both magnitude and duration. For events originating from Merapi with such source characteristics (VT-B, MP, and LF), small variations in event duration (in BPPTKG catalogue) corresponded to greater variations in the detection duration (Fig. 8b). We interpret this as indicating that the 0.8–1.8 Hz band captures a significant portion of the main energy content for these event categories, such that the scaling behaviour predictably produces longer durations for higher-magnitude events. The propagating signals are subsequently affected by scattering along their paths, which further increases the observed durations at the array.

For tectonic events, the comparison between durations measured at BPPTKG stations and those measured at our array should be more directly proportional, since the Merapi–array distance is smaller than the source–station distance. Consequently, the path effects influencing both recordings are expected to be broadly similar. The remaining variability may result from a combination of factors, including differences in source–station distance, signal directionality, medium heterogeneity, site effects, variations in recording instruments, and the fact that the 0.8–1.8 Hz band may not always represent the dominant spectral content of the events.

article in press

Rockfall events are generated at the surface by moving materials and rock masses, where the interaction between the mass and the ground produces complex and unpredictable waveform characteristics. The resulting surface waves are subject to stronger scattering and attenuation due to near-surface heterogeneity, reduced material compaction, and terrain roughness. Consequently, it is difficult to identify a consistent pattern that defines the duration of these events. A similar explanation applies to pyroclastic flow events, which involve more intense and prolonged source process as the flow moves along the surface. These characteristics yield extended and variable durations that are less directly comparable with the more impulsive volcanic or tectonic sources.

Implications of characterization and classification

The comparison between characterization parameters shows that weight and the elevation-based parameter provide the clearest separation between tectonic and VT-B detections. This result does not yet represent a complete classification method, but it provides a useful basis for evaluating whether simple automatic classification could be developed from the characterization parameters.

As an initial experiment, we defined simple threshold criteria for all characterization parameters. The thresholds were manually selected to maximize the separation of volcanic from tectonic detections (Fig. 12), and were defined as follows: mean apparent velocity < 4 km/s, standard deviation of back-azimuth < 100 degrees, mean weight > 0.12, and mean elevation-based parameter > -1 km. The inclusion of detection duration was treated as optional, depending on whether pyroclastic flow events were to be included in the volcanic category. When only shorter-duration events were of interest, an additional criterion of detection duration < 160 s was applied, which excludes our longest pyroclastic flow but potentially identifies a larger number of detections as volcanic.

In the BPPTKG catalogue, we grouped VT-B, MP, LF, rockfall, and pyroclastic flow events into the volcanic category, while non-volcanic category comprised tectonic and other types. Using our threshold criteria, 432 of 1,677 detections (25.76%) were classified as volcanic, representing a 4.35% increase compared to the 414 volcanic events matched with the BPPTKG catalogue. Among the 637 matched detections, 276 (43.33%) were correctly classified as volcanic, corresponding to a 33.33% decrease relative to the matched volcanic events in the catalogue. A total of 138 volcanic events from the BPPTKG catalogue were misclassified as non-volcanic, while 156 previously unclassified detections that were not matched with catalogue events were newly categorized as volcanic. Most of the misclassified detections corresponded to MP, LF, and rockfall events, which could not be reliably distinguished from other categories in this multi-parameter comparison. In contrast, 202 of 214 matched VT-B

article in press

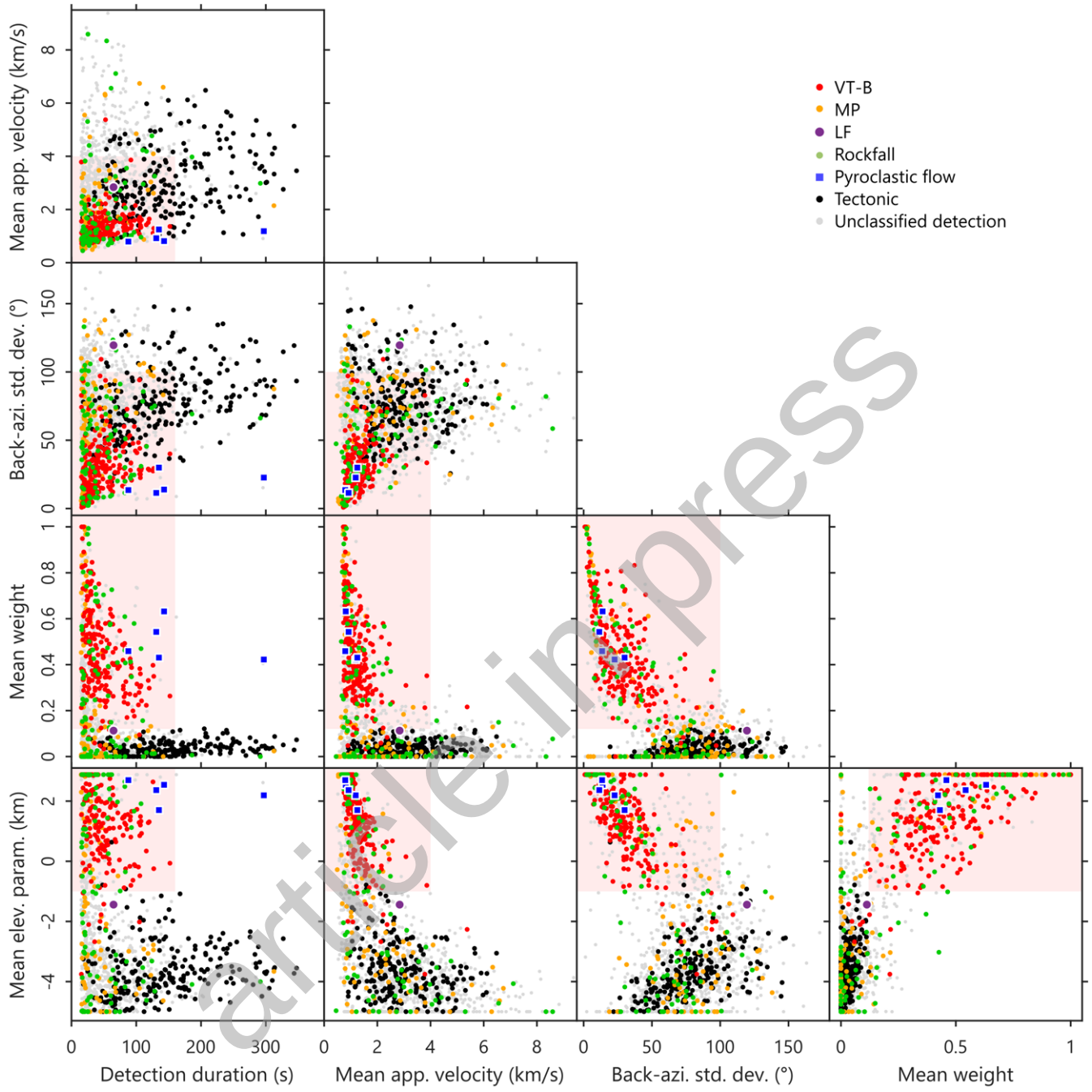
events (94.39%) satisfied the volcanic classification criteria, demonstrating that our detection and characterization methods are most effective at identifying VT-B events or signals with VT-B characteristics.

This thresholding experiment should be viewed as a rudimentary test of future automatic classification rather than as a main result of the present study. The comparison shows why the overall volcanic classification performance remains limited. MP, LF, and rockfall events overlapped substantially with tectonic and unclassified detections, whereas VT-B events formed a more distinct group. Thus, the main value of this experiment is not the simple classification itself, but the confirmation that some characterization parameters are already consistent enough with the BPPTKG catalogue to guide more advanced classification in future work.

The increase in apparent velocity with $\max\langle E\rangle_S$ may reflect the dominance of faster seismic waves during the earliest arrivals, whereas the higher uncertainty in back-azimuth estimation is less straightforward to explain, particularly given the narrow frequency band and limited spatial resolution of our array. Increasing waveform complexity and differing dominant frequencies of the faster phases may have contributed to greater variability in both apparent velocity and back-azimuth during the first half of the detection duration, a behaviour most evident in tectonic events and possibly in our single matched LF event (Figs. 5m–n).

The absence of clear relationships between $\max\langle E\rangle_S$ and the mean elevation-based parameter or mean weight reflects their stronger dependence on event category than on event magnitude. Their values, particularly for tectonic and VT-B events, tend to cluster in different parts of the elevation and weight ranges regardless of magnitude. Nevertheless, higher-magnitude VT-B events tended to be associated with lower weights, mainly because these events showed larger back-azimuth deviations from north, corresponding to lower values in the weighting scheme. These results indicate that more advanced classification of characterization values is feasible, particularly to distinguish VT-B and potentially pyroclastic flow events from tectonic events. With further development, such approaches could also enable differentiation among individual volcanic event types. Implementing these methods using probabilistic or non-probabilistic approaches (e.g., Ester et al. 1996; Zheng et al. 2021), is well within reach, though this was beyond the scope of the present study.

article in press



article in press

Figure 12: Comparison between detection duration and characterization parameters (mean apparent velocity, standard deviation of back-azimuth, mean weight, and mean elevation-based parameter) for 1,677 detections, including detections matched with the BPPTKG catalogue and unclassified detections. Red-shaded areas indicate exploratory value ranges used to evaluate the possibility of simple volcanic event classification.

Interpretation of volcanic activity

The temporal evolution of volcanic events during our observation period in 2023 is primarily constrained by the BPPTKG catalogue, while our array provides a reduced and independent view of the same period (Figs. 6–7). The official catalogue suggests a phase of volcanic unrest consistent with the known effusive behaviour of Merapi (Ratdomopurbo and Poupinet 2000). This behaviour is typically characterized by lava-dome growth, collapses generating pyroclastic flows, and occasional short-lived explosive phases (Surono et al. 2012; Voight et al. 2000). Previous Merapi seismic studies have also related changes in shallow seismicity and seismic velocity to magma migration, stress changes, and damage or healing within the shallow edifice before eruption (Budi-Santoso and Lesage 2016). Comparable dome-growth and partial-destruction behaviour has also been documented at Volcan de Colima, where lava effusion, lava flows, rockfalls, Vulcanian explosions, pyroclastic density currents, SO2 flux, seismic energy, frequency-index changes, and seismic-event families were used together to interpret the transition from effusive activity to dome destruction (Arámbula-Mendoza et al. 2025). Although our array detected only a smaller subset of the catalogue, its matched detections still reproduced several coarse features of this temporal evolution, including the early-July and early-December unrest peak. Therefore, the interpretation below is not based solely on our array, but our results show that a more rudimentary version of the same activity pattern can be recovered from the low-cost, distant array.

Previous studies have proposed that groundwater can be a key factor influencing eruptive processes, in addition to the ascent of magmatic fluids from depth (e.g., Carn et al. 2004; Farquharson and Amelung 2020). At shallow depths, the abundant supply of meteoric water from rainfall may contribute to the triggering of eruptive or dome-collapse episodes through structural weakening by increased pore pressure or hydrothermal alteration, as well as by landslide initiation on steep slopes (e.g., Carn et al. 2004; Farquharson and Amelung 2020). As contextual information for this interpretation, we compared the temporal distribution of volcanic events with rainfall near Merapi summit derived from the ERA5-Land reanalysis dataset (Fig. 6g).

Our interpretation of the temporal evolution of volcanic processes at Merapi during the data period considers three approximate domains: the subsurface, encompassing the internal volcanic structure up to about 1 km beneath the vent; the near-surface, representing the shallow edifice above this depth and up to the surface; and the surface, referring to processes occurring directly on or above the ground. Rather than discussing each domain independently, we integrate processes across these domains to provide a coherent interpretation of the observed activity.

article in press

The distribution of volcanic events (Figs. 6a–e) indicates a main unrest episode that we interpret as reflecting progressive shallow volcanic unrest, broadly consistent with magma supply or pressurization processes at depths shallower than 1.5 km, following the BPPTKG event classification and previous Merapi seismic interpretations (Ratdomopurbo and Poupinet 2000; Budi-Santoso and Lesage 2016). Such shallow unrest may involve pressurization of the volcanic conduit system, which could promote brittle fracturing of the surrounding rocks and be expressed as VT-B events. Surono et al. (2012) also suggested that increases in LF activity reflect elevated gas influx or the presence of superheated water ascending from depth. However, shallow long-period seismicity can also be generated by propagation-path effects, deformation, or slow rupture in weak volcanic materials (Bean et al. 2014), so the LF occurrence is treated here as an indicator of shallow volcanic unrest rather than a unique constraint on the fluid pathway. As magma approached the surface and accumulated near the vent, it contributed to dome-building process (MP events), depositing new viscous lava that increase the obstruction of the conduit. This inferred dome-building process may have increased conduit obstruction, allowing shallow pressurization to persist and contributing to the prolonged unrest, consistent with the role of shallow conduit processes during dome growth and collapse episodes (Cassidy et al. 2018). Concurrently, rockfall events are interpreted as minor gravitational collapse of unstable dome material. Such a coupling between dome growth, rockfall occurrence, and seismicity was also observed during the 2016–2017 activity at Volcan de Colima (Arámbula-Mendoza et al. 2025).

We suggest that surface interaction with rainwater may have accelerated lava cooling as the rainfall intensity increased toward the end of November (Fig. 6g). Accelerated cooling likely enhanced vent blockage, promoting pressure buildup from heated fluids (magma, gas, and water) beneath the solidifying lava. From late November to early December, coinciding with the peak rainfall, we interpret that a sufficient amount of water had infiltrated the shallow subsurface, intensifying groundwater interaction with the magma. The buildup of gas from magma degassing and groundwater conversion helped weaken the dome integrity, initiating a phreatomagmatic phase. More generally, transitions between effusive and explosive behaviour during a single eruptive phase can occur during dome growth and collapse episodes, and are commonly controlled by shallow conduit processes (Cassidy et al. 2018).

One or more phreatic explosions may have occurred during this phase, fracturing and further destabilizing the dome and triggering pyroclastic flows. Additional pyroclastic flows likely occurred from gravitational collapses of the unstable dome material, many of which were smaller in magnitude and recorded as increases in rockfall activity. Following the major dome-collapse episode in early December, the accumulated pressure was released, allowing gases to escape more freely through the vent and relieving the shallow magmatic–hydrothermal system. The remaining dome material subsequently reached a more stable state.

article in press

Comparison with rainfall and the observed tectonic event occurrences suggests that non-volcanic factors played a significant role during this unrest episode. In early July, magma supply and dome-building processes were likely interrupted by a brief, less-intense rainfall episode, which partially collapsed the dome and delayed further pressure buildup until early August. This stage was less extensive than the subsequent one, and the stabilization of rockfall occurrences after the rapid early-July increase suggests that the dome structure remained largely intact.

A short-lived VT-B swarm also occurred during the two collapse episodes, which we interpret as disturbances within the very shallow structure, where pressurized fluids in the fracture network struggled to reach the surface. The more intense VT-B activity during the earlier partial collapse, together with the comparatively lower pyroclastic-flow activity, suggests that pressure release through the vent was slower and more restricted than during the December collapse. Based on this, we infer that the contribution of phreatomagmatic process during the earlier episode was likely less significant.

The tectonic peaks in late June and early December (Fig. 6f) occurred near the two interpreted collapse episodes. Although these activity peaks occurred within short time intervals, we cannot confidently infer whether tectonic shaking directly influenced dome stability, as we did not evaluate the energy release of the tectonic events. Nevertheless, the possibility that combined tectonic and meteorological factors modulate lava dome evolution at Merapi highlights the importance of investigating volcano–tectonic interactions and improving volcano monitoring strategies. This is particularly relevant given the presence of the nearby active Opak Fault, which has been suggested to influence Merapi's eruptive processes (Saputra et al. 2021; Wagner et al. 2007).

Summary on unclassified detections

The sources of unclassified signals remain difficult to determine, as signals unrelated to volcanic activity, such as false detections, environmental disturbances, or anthropogenic noise, may be involved. Although some detections may originate from volcanic processes, they could not be confirmed through the official BPPTKG catalogue during the observation period.

We isolated 1,036 unclassified detections and examined their characteristics following the analyses presented in Figs. 9 and 10. To evaluate possible temporal changes in their behaviour, we divided them into three periods based on patterns observed in Fig. 6h: (1) 27 June–30 September, when unclassified detections occurred at a stable average rate of 2.39 events per day; (2) 1 October–31 December excluding 1–5 December; and (3) 1–5 December, during which a sharp peak of 79 detections in a single day was recorded. These analyses integrate the characterization patterns and signal-shape comparisons of unclassified detections with their temporal occurrence.

article in press

We also manually inspected the signal shapes of all 1,036 unclassified detections. Assuming that volcanic seismic energy should be mainly contained within the first half of the detection duration, only 100 detections (9.65%) roughly resembled the volcanic examples. These consisted of 38 detections during 27 June–30 September, 44 detections during 1 October–31 December excluding 1–5 December, and 18 detections during 1–5 December. These detections may be considered possible volcanic candidates, but they remain difficult to classify because their characterization values are uncertain. In addition, anthropogenic signals may also show an impulsive onset followed by decaying amplitude, resembling an earthquake-like signal.

The comparison results focusing on the unclassified detections are provided in Fig. S3 in the Supplementary Material. Despite exhibiting characteristics similar to many MP and rockfall events, and with 156 detections satisfying our volcanic classification criteria, their generally small magnitudes and lack of corresponding entries in the BPPTKG catalogue make a volcanic origin difficult to confirm. The difference between the 156 detections satisfying the threshold criteria and the 100 detections with volcanic-like signal shapes illustrates the uncertainty of using simple thresholds for unclassified detections. Moreover, the MP and rockfall categories themselves could not be reliably distinguished using our array, further complicating the interpretation. We found no systematic differences between unclassified detections occurring before October and those occurring afterward. Detections recorded between 1–5 December tended to exhibit higher inferred magnitudes than those occurring since October, suggesting a notable change in the underlying signal sources during this brief period.

A comparison of signal shapes analogous to Fig. 10 was also conducted for the three time periods of unclassified detections (Fig. S3). In general, the linear relationship between detection duration and $\max\langle E\rangle_S$ was poorly evident, and the signal envelopes were more irregular than those of MP and rockfall events (Figs. 10b and d). Unclassified detections occurring after October exhibited a broader range of magnitudes than those from earlier months, suggesting increased variability in either source strength or source mechanism. During 1–5 December, we identified several pairs of detections with similar magnitudes, durations, and envelope shapes. We interpret these twin events as repeating signals generated by artificial or anthropogenic sources near the array. We consider it unlikely that multiple volcanic events would have nearly matching amplitude levels and signal shapes, especially given the limited resolution of the array. The specific origins cannot be confirmed, as no detailed log of nearby human activities was available during the deployment period.

We also noted temporal correspondence with the peak in tectonic event occurrences in early December. We considered the possibility that some unclassified detections from this interval may represent unconfirmed or partial tectonic signals. Note that the BPPTKG catalogue does not provide detailed focal parameters for tectonic events, and distinguishing volcanic from tectonic signals recorded by the local Merapi network is often challenging. To

article in press

facilitate rapid classification, BPPTKG typically compares the seismic recordings at Merapi with those from an additional station located approximately 48 km south from Merapi, closer to the Opak Fault. Tectonic events are expected to be detected at both sites within a short time interval, enabling quick discrimination. However, this approach remains sensitive to technical errors or unrelated signals at the distant station, both of which can lead to misidentification. It is also possible that minor activity along the Opak Fault was inadvertently compared with volcanic signals, but this is purely speculative.

The increase in unclassified detections from October onward appears broadly consistent with the period of intensified MP activity (Fig. 7). However, among the volcanic events detected by our array, VT-B events were the most clearly resolved, and the increase in unclassified detections did not correlate clearly with the VT-B activity (Figs. 6a and 6h). The unclassified detection counts also show some temporal correspondence with pyroclastic flows and tectonic events (Fig. 6), but their causal relationships remain inconclusive because these detections were not matched with catalogue events. Instead, another possible explanation comes from the temporal correspondence with the sustained rainfall episode. We could not confirm whether rainfall itself generated distinguishable seismic energy, as no local rainfall occurrence logs were available near the array. Given the array location within a settlement area, the increase in unclassified detections during the later part of the observation period may also reflect changes in anthropogenic activity in response to precipitation, rather than direct rainfall-generated seismic sources.

Context for future developments

In this study, we presented the results of an experimental seismic monitoring effort using a suboptimal array configuration. Our methodology was deliberately designed to address the inherent limitations of the array when applied to Merapi monitoring, with many parameters fine-tuned specifically for this case. Despite these constraints, our results show that the array could still detect and characterize the strongest VT-B events, identify most matched tectonic events, distinguish VT-B-like signals from tectonic events using weight and the elevation-based parameter, and quantify how station availability affects back-azimuth stability. These results are useful not because they provide a catalogue that is more complete than the official one, but because they define what information remains recoverable when the array geometry and site conditions are far from ideal. Accordingly, this study provides a rare and valuable evaluation of a scenario in which limitations are dominant, rather than an ideal, near-textbook case in which they have been largely mitigated. This evaluation is not intended to suggest that a distant array is preferable

article in press

to a proximal monitoring network. Rather, it addresses a practical question that may arise when closer deployment is limited by access, maintenance, safety, logistics, or available resources: what level of seismic information can still be recovered from a suboptimal configuration, and which limitations should be expected?

Our array experiment continues to operate, and future developments are expected to include the deployment of additional low-cost arrays and local stations positioned closer to Merapi. Increasing the number of seismic stations, particularly with improved azimuthal coverage and varying source–receiver distances, will enhance the precision of source location estimates while addressing the difficulties of conventional methods. This improvement can be achieved by refining coherence-based methods, such as those demonstrated in this study, and by incorporating spatial amplitude attenuation models that account for both geometrical spreading and intrinsic attenuation (e.g., Battaglia and Aki 2003; Permana and Aoyama 2023). Further quantitative amplitude analyses will also require calibration for site effects, propagation paths, and attenuation.

Ultimately, these advancements will improve the reliability of volcanic catalogues and support more detailed investigations of the temporal evolution of seismic activity. In addition, combining seismic observations with infrasound data will be essential to fully exploit the dual-sensor capability of RS&BOOM instruments. Integrating complementary datasets, such as detailed tectonic event catalogues, high-resolution rainfall measurements, and other non-seismic monitoring data, represents a promising direction for advancing the understanding of volcanic activity and refining low-cost volcano monitoring strategies. Such integration of conventional monitoring, low-cost instruments, and complementary observations has also been highlighted by recent volcano-monitoring applications (Clive et al. 2024).

Conclusions

This study assessed the feasibility of seismicity monitoring of Merapi Volcano using a Raspberry Shake RS&BOOM array situated at a suboptimal distance of approximately 17 km from the summit. Despite this suboptimal distance and array configuration, the median-based detection method and the set of characterization parameters developed here (apparent velocity, back-azimuth stability, back-azimuth-derived weight, and an elevation-based parameter) recovered several forms of information from the narrow 0.8–1.8 Hz band: the timing of the strongest VT-B events, a reduced temporal pattern of volcanic activity relative to the BPPTKG catalogue, the separation of many tectonic and VT-B-like signals, and the dependence of back-azimuth stability on station availability. However, only 637 of 1,677 detections were matched with the BPPTKG catalogue, while 1,036

article in press

detections remained unclassified, confirming that the array provides only a reduced and complementary view of Merapi seismicity.

Among the characterization metrics, the elevation-based parameter and weight provided the clearest distinction between tectonic and VT-B-like events, providing a basis for exploratory automatic classification. Detection duration and maximum short-window median amplitude scaled well with VT-B event magnitude, offering potential for basic magnitude estimation under limited conditions. Meanwhile, the large number of unclassified detections may reflect a mixture of small volcanic, anthropogenic, environmental, and possibly tectonic signals. Manual inspection showed that only 100 of the 1,036 unclassified detections roughly resembled volcanic examples, and their origins remain uncertain. Peaks in unclassified detections coincided with heightened volcanic activity, intense rainfall, and increased tectonic events, highlighting the difficulty of interpreting seismicity at a distance, within a reduced frequency band, and without direct catalogue matches.

Oversampling improved the stability of characterization parameters by allowing finer numerical time shifting, but it did not improve the original timing accuracy and could not overcome the small-aperture limitation of the array. Station availability tests further showed that back-azimuth estimates deteriorate substantially when fewer than five stations are operational. Overall, while such a low-cost, distant array cannot replace the dedicated proximal monitoring network at Merapi, it can still provide meaningful complementary constraints when paired with tailored processing strategies. Therefore, the main value of this study is to quantify both the capability and the limitation of an imperfect but practical monitoring configuration, rather than to propose it as an alternative to dedicated proximal instrumentation. Expanding low-cost deployments, integrating seismic and infrasound data, and applying multi-parameter or machine-learning approaches will further enhance the capability of low-cost networks to monitor volcanoes with limited resources.

Author contributions

Weber and Suryanto managed the entirety of the array experiment project. Anggraini and Yuliantoro coordinated the field efforts, including the installation and maintenance of the array. Permana designed the analyses, performed the computations, and led the manuscript preparation. Irnaka and Darmawan managed the array data and contributed to additional analyses and general discussion. Santoso maintained the Merapi event catalogue and provided complementary data and interpretations related to Merapi. All authors contributed to the preparation of the manuscript.

article in press

Acknowledgements

We thank Wolfgang Kohl and his team, as well as the members of the Geophysics Laboratory, Universitas Gadjah Mada, for their efforts in installing and maintaining the array. This study was supported by the Direktorat Penelitian Universitas Gadjah Mada (Directorate of Research, Universitas Gadjah Mada) through the Program Asistensi Riset Tahun Anggaran 2025 (2025 Research Assistance Program), Contract No. 4588/UN1.P4/Dit-Lit/PT.01.03/2025. We are grateful for the valuable discussion with Novia Antika, Nanang Sugianto, Andika Bayu Aji, Thystere Matondo Bantidi, and Lorène Boulvais-Abbas. We also thank the editors and two anonymous reviewers for their constructive comments, which helped us improve the manuscript.

Data availability

The experimental seismic array data used in this study are not currently available to the public. However, two weeks of raw seismic data from all five RS&BOOM array stations, covering 26 August–8 September 2023, and the full detection catalogue produced in this study are available through Zenodo at https://doi.org/10.5281/zenodo.20570927. The Merapi event catalogue should be obtained directly from the Balai Penyelidikan dan Pengembangan Teknologi Kebencanaan Geologi (BPPTKG). Information on Indonesian volcanic monitoring networks is publicly accessible through the Portal Mitigasi Bencana Geologi (Portal MBG, https://vsi.esdm.go.id/portalmbg), maintained by the Centre for Volcanology and Geological Hazard Mitigation (PVMBG). The tectonic earthquake catalogue from the Indonesian Agency for Meteorology, Climatology, and Geophysics (BMKG) is available at https://repogempa.bmkg.go.id. The CRUST 1.0 model (Laske et al. 2013) can be accessed at https://igppweb.ucsd.edu/~gabi/crust1.html. The map in Fig. 1 utilized several open datasets: the DEMNAS elevation data from the Indonesian Geospatial Information Agency (BIG) available at https://tanahair.indonesia.go.id/portal-web/unduh; global topography and bathymetry data from the NASA Shuttle Radar Topography Mission (2013) accessed via OpenTopography (https://doi.org/10.5069/G9445JDF); and the LandScan Global population density data from the Oak Ridge National Laboratory (Lebakula et al. 2024) available at https://landscan.ornl.gov. The ERA5-Land reanalysis dataset (Muñoz Sabater 2025) is available through the Copernicus Climate Change Service (C3S) Climate Data Store (CDS) at https://cds.climate.copernicus.eu.

References

article in press

Allard, P., Métrich, N., & Sabroux, J.-C. (2011). Volatile and magma supply to standard eruptive activity at Merapi volcano, Indonesia. *EGU General Assembly Conference Abstracts*, *13*, EGU2011-13522. https://meetingorganizer.copernicus.org/EGU2011/EGU2011-13522.pdf

Allen, R. V. (1978). Automatic earthquake recognition and timing from single traces. *Bulletin of the Seismological Society of America*, *68*(5), 1521–1532. https://doi.org/10.1785/BSSA0680051521

Arámbula-Mendoza, R., García-Flores, R. de J., Varley, N., Campion, R., Vargas-Bracamontes, D. M., González-Amezcua, M., & Martínez-Fierros, A. (2025). Study of lava dome growth and its partial destruction during September 2016 to February 2017 at Volcan de Colima, Mexico. *Journal of South American Earth Sciences*, *161*(1), 105577. https://doi.org/10.1016/j.jsames.2025.105577

Battaglia, J., & Aki, K. (2003). Location of seismic events and eruptive fissures on the Piton de la Fournaise volcano using seismic amplitudes. *Journal of Geophysical Research: Solid Earth*, *108*(B8), 2364. https://doi.org/10.1029/2002JB002193

Bean, C. J., De Barros, L., Lokmer, I., Métaxian, J.-P., O'Brien, G. S., & Murphy, S. (2014). Long-period seismicity in the shallow volcanic edifice formed from slow-rupture earthquakes. *Nature Geoscience, 7*(1), 71–75. https://doi.org/10.1038/ngeo2027

Budi-Santoso, A., & Lesage, P. (2016). Relative seismic velocity variations during the Merapi 2010 eruption recorded by seismic multiplets and ambient noise cross-correlation. *Geophysical Journal International, 206*(1), 221–240. https://doi.org/10.1093/gji/ggw145

Carn, S. A., Watts, R. B., Thompson, G., & Norton, G. E. (2004). Anatomy of a lava dome collapse: The 20 March 2000 event at Soufrière Hills Volcano, Montserrat. *Journal of Volcanology and Geothermal Research*, *131*(3–4), 241–264. https://doi.org/10.1016/S0377-0273(03)00364-0

Cassidy, M., Manga, M., Cashman, K., & Bachmann, O. (2018). Controls on explosive-effusive volcanic eruption styles. *Nature Communications, 9*(1), 2839. https://doi.org/10.1038/s41467-018-05293-3

Charbonnier, S. J., & Gertisser, R. (2008). Field observations and surface characteristics of pristine block-and-ash flow deposits from the 2006 eruption of Merapi volcano, Java, Indonesia. *Journal of Volcanology and Geothermal Research*, *177*(4), 971–982. https://doi.org/10.1016/j.jvolgeores.2008.07.008

Clive, M. A. T., Lawson, R. V., Lamb, O. D., Potter, S., Kilgour, G., Jarvis, P. A., Harrison, S., Scott, B., & Charlton, D. (2024). Crowdsourcing human observations expands and enhances volcano monitoring records. *Communications Earth & Environment, 5*(1), 599. https://doi.org/10.1038/s43247-024-01747-3

article in press

Deegan, F. M., Troll, V. R., Freda, C., Misiti, V., & Chadwick, J. P. (2011). Fast and furious: Crustal CO_2 release at Merapi volcano, Indonesia. *Geology Today*, *27*(2), 63–64. https://doi.org/10.1111/j.1365-2451.2011.00785.x

Droznin, D. V., Shapiro, N. M., Droznina, S. Y., Senyukov, S. L., Chebrov, V. N., & Gordeev, E. I. (2015). Detecting and locating volcanic tremors on the Klyuchevskoy group of volcanoes (Kamchatka) based on correlations of continuous seismic records. *Geophysical Journal International*, *203*(2), 1001–1010. https://doi.org/10.1093/gji/ggv342

Eibl, E. P. S., Bean, C. J., Vogfjörd, K. S., Ying, Y., Lokmer, I., Möllhoff, M., O'Brien, G. S., & Pálsson, F. (2017). Tremor-rich shallow dyke formation followed by silent magma flow at Bárðarbunga in Iceland. *Nature Geoscience, 10*(4), 299–304. https://doi.org/10.1038/ngeo2906

Ester, M., Kriegel, H.-P., Sander, J., & Xu, X. (1996). A density-based algorithm for discovering clusters in large spatial databases with noise. In *Proceedings of the Second International Conference on Knowledge Discovery and Data Mining (KDD-96)* (pp. 226–231). AAAI Press.

Farquharson, J. I., & Amelung, F. (2020). Extreme rainfall triggered the 2018 rift eruption at Kīlauea Volcano. *Nature*, *580*(7803), 491–495. https://doi.org/10.1038/s41586-020-2172-5

Friedrich, A., Krüger, F., & Klinge, K. (1998). Ocean-generated microseismic noise located with the Gräfenberg array. *Journal of Seismology*, *2*(1), 47–64. https://doi.org/10.1023/A:1009788904007

Goebel, T. H. W., Thapa, N., Rinty, S. M., Andino, S. D., Martinez-Coto, A., Rivera, J., & Henriquez-Miranda, B. (2025). A community seismic network for the early detection of seismic activity close to active volcanoes in western El Salvador. *Seismological Research Letters, 96*(4), 2241–2252. https://doi.org/10.1785/0220240343

Hasselmann, K. (1963). A statistical analysis of the generation of microseism. *Reviews of Geophysics*, *1*(2), 123–282. https://doi.org/10.1029/RG001i002p00177

Hata, M., Nishimura, T., Matsushima, T., Kozono, T., Nagatsuma, T., Murata, K. T., Kikuta, K., Muramatsu, D., & Nakahara, H. (2024). Volcanic tremor associated with successive gas emission activity at a boiling pool: Analyses of seismic array and visible image data recorded at Iwo-Yama in Kirishima volcanic complex, Japan. *Journal of Volcanology and Geothermal Research*, *455*(1), 108212. https://doi.org/10.1016/j.jvolgeores.2024.108212

Hidayati, S., Ishihara, K., & Iguchi, M. (2007). Volcano-tectonic earthquakes during the stage of magma accumulation at the Aira Caldera, southern Kyushu, Japan. *Bulletin of the Volcanological Society of Japan*, *52*(6), 289–309. https://doi.org/10.18940/kazan.52.6_289

article in press

Hirata, N., & Matsu'ura, M. (1987). Maximum-likelihood estimation of hypocenter with origin time eliminated using nonlinear inversion technique. *Physics of the Earth and Planetary Interiors*, *47*(1), 50–61. https://doi.org/10.1016/0031-9201(87)90066-5

Hutchings, S. J., & Mooney, W. D. (2021). The seismicity of Indonesia and tectonic implications. *Geochemistry, Geophysics, Geosystems*, *22*(9), e2021GC009812. https://doi.org/10.1029/2021GC009812

International Association of Volcanology and Chemistry of the Earth's Interior. (1996). *Decade volcanoes* (*IAVCEI News*, 1/2). IAVCEI. https://www.iavceivolcano.org/content/uploads/2020/09/iavcei-newsletter-1996-no-1.pdf

Irsyam, M., Widiyantoro, S., Natawidjaja, D. H., Meilano, I., Rudyanto, A., Hidayati, S., Triyoso, W., Hanifa, N. R., Djarwadi, D., Faizal, L., & Sunarjito. (2017). *Peta sumber dan bahaya gempa Indonesia tahun 2017* [Seismic source and hazard map of Indonesia 2017]. Kementerian Pekerjaan Umum dan Perumahan Rakyat.

Journeau, C., Shapiro, N. M., Seydoux, L., Soubestre, J., Koulakov, I. Y., Jakovlev, A. V., Abkadyrov, I., Gordeev, E. I., Chebrov, D. V., Droznin, D. V., Sens-Schönfelder, C., Luehr, B. G., Tong, F., Farge, G., & Jaupart, C. (2022). Seismic tremor reveals active trans-crustal magmatic system beneath Kamchatka volcanoes. *Science Advances*, *8*(5), eabj1571. https://doi.org/10.1126/sciadv.abj1571

Koulakov, I., Bohm, M., Asch, G., Lühr, B.-G., Manzanares, A., Brotopuspito, K. S., Fauzi, P., Purbawinata, M. A., Puspito, N. T., Ratdomopurbo, A., Kopp, H., Rabbel, W., & Shevkunova, E. (2007). P and S velocity structure of the crust and the upper mantle beneath Central Java from local tomography inversion. *Journal of Geophysical Research: Solid Earth*, *112*(B8), B08310. https://doi.org/10.1029/2006JB004712

Lavigne, F., Thouret, J.-C., Voight, B., Suwa, H., & Sumaryono, A. (2000). Lahars at Merapi volcano, Central Java: An overview. *Journal of Volcanology and Geothermal Research*, *100*(1–4), 423–456. https://doi.org/10.1016/S0377-0273(00)00150-5

Laske, G., Masters, G., Ma, Z., & Pasyanos, M. (2013). Update on CRUST1.0: A 1-degree global model of Earth's crust. *EGU General Assembly Conference Abstracts*, *15*, EGU2013-2658.

Lebakula, V., Epting, J., Moehl, J., Stipek, C., Adams, D., Reith, A., Kaufman, J., Gonzales, J., Reynolds, B., Basford, S., Martin, A., Buck, W., Faxon, A., Cunningham, A., Roy, A., Barbose, Z., Massaro, J., Walters, S., Woody, C., … Urban, M. (2024). *LandScan Silver Edition* [Data set]. Oak Ridge National Laboratory. https://doi.org/10.48690/1531770

Lesage, P., Heap, M. J., & Kushnir, A. (2018). A generic model for the shallow velocity structure of volcanoes. *Journal of Volcanology and Geothermal Research*, *356*, 114–126. https://doi.org/10.1016/j.jvolgeores.2018.03.003

article in press

Lomax, A., Michelini, A., & Curtis, A. (2008). Earthquake location, direct, global-search methods. In R. A. Meyers (Ed.), *Encyclopedia of complexity and systems science* (pp. 2449–2473). Springer. https://doi.org/10.1007/978-3-642-27737-5_150-2

Maeda, N. (1985). A method for reading and checking phase time in auto-processing system of seismic wave data. *Journal of the Seismological Society of Japan. Second Series*, *38*(3), 365–379. https://doi.org/10.4294/zisin1948.38.3_365

Muñoz Sabater, J. (2025). *ERA5-Land hourly time-series data on single levels from 1950 to present* [Data set]. Copernicus Climate Change Service (C3S) Climate Data Store (CDS). https://doi.org/10.24381/cds.e2161bac

NASA Shuttle Radar Topography Mission. (2013). *Shuttle Radar Topography Mission (SRTM) global* [Data set]. OpenTopography. https://doi.org/10.5069/G9445JDF

Nishimura, T., & Iguchi, M. (2011). *Volcanic earthquakes and tremor in Japan*. Kyoto University Press.

Ogiso, M., & Tamaribuchi, K. (2022). Spatiotemporal evolution of tremor activity near the Nankai Trough trench axis inferred from the spatial distribution of seismic amplitudes. *Earth, Planets and Space*, *74*(1), 49. https://doi.org/10.1186/s40623-022-01601-w

Permana, T., & Aoyama, H. (2023). Locating volcanic earthquakes and tremors using delay time and amplitude ratio information from cross-correlation functions. *Seismological Research Letters*, *94*(2A), 871–886. https://doi.org/10.1785/0220220199

Permana, T., Nishimura, T., Nakahara, H., Fujita, E., & Ueda, H. (2020). Reliability evaluation of volcanic tremor source location determination using cross-correlation functions. *Geophysical Journal International*, *220*(2), 1300–1315. https://doi.org/10.1093/gji/ggz523

Permana, T., Nishimura, T., Nakahara, H., & Shapiro, N. M. (2022). Classification of volcanic tremors and earthquakes based on seismic correlation: Application at Sakurajima volcano, Japan. *Geophysical Journal International*, *229*(2), 1077–1097. https://doi.org/10.1093/gji/ggab517

Permana, T., Yatimantoro, T., & Handayani, A. S. (2023). Seismic signature detection during the 2018 Anak Krakatau flank collapse and tsunami using seismic amplitudes from regional-scale monitoring. *Earth, Planets and Space*, *75*(1), 162. https://doi.org/10.1186/s40623-023-01917-1

Ratdomopurbo, A., & Poupinet, G. (2000). An overview of the seismicity of Merapi volcano (Java, Indonesia), 1983–1994. *Journal of Volcanology and Geothermal Research*, *100*(1–4), 193–214. https://doi.org/10.1016/S0377-0273(00)00137-2

article in press

Reiller, H., Bani, P., Dupont, A., Wendling, N., Legrand, D., Battaglia, J., Peter, E., & William, R. (2026). Raspberry infrasound and seismic sensors: A new perspective for volcano research and monitoring—the case of Yasur. *Bulletin of Volcanology, 88*(3), 21. https://doi.org/10.1007/s00445-026-01940-6

Rost, S., & Thomas, C. (2002). Array seismology: Methods and applications. *Reviews of Geophysics, 40*(3), 1008. https://doi.org/10.1029/2000RG000100

Saputra, H., Wahyudi, W., Suardi, I., Anggraini, A., & Suryanto, W. (2021). The waveform inversion of mainshock and aftershock data of the 2006 M6.3 Yogyakarta earthquake. *Geoscience Letters*, *8*(1), 9. https://doi.org/10.1186/s40562-021-00176-w

Schweitzer, J., Fyen, J., Mykkeltveit, S., Gibbons, S. J., Pirli, M., Kühn, D., & Kværna, T. (2012). Seismic arrays. In P. Bormann (Ed.), *New manual of seismological observatory practice (NMSOP-2)* (pp. 1–80). Deutsches GeoForschungsZentrum GFZ. https://doi.org/10.2312/GFZ.NMSOP-2_ch9

Sens-Schönfelder, C., & Wegler, U. (2006). Passive image interferometry and seasonal variations of seismic velocities at Merapi volcano, Indonesia. *Geophysical Research Letters*, *33*(21), L21302. https://doi.org/10.1029/2006GL027797

Seydoux, L., Shapiro, N. M., de Rosny, J., Brenguier, F., & Landes, M. (2016). Detecting seismic activity with a covariance matrix analysis of data recorded on seismic arrays. *Geophysical Journal International*, *204*(3), 1430–1442. https://doi.org/10.1093/gji/ggv531

Surono, Jousset, P., Pallister, J., Boichu, M., Buongiorno, M. F., Budisantoso, A., Costa, F., Andreastuti, S., Prata, F., Schneider, D., Clarisse, L., Humaida, H., Sumarti, S., Bignami, C., Griswold, J., Carn, S., Oppenheimer, C., & Lavigne, F. (2012). The 2010 explosive eruption of Java's Merapi volcano—A "100-year" event. *Journal of Volcanology and Geothermal Research*, *241–242*(1), 121–135. https://doi.org/10.1016/j.jvolgeores.2012.06.018

Tiede, C., Camacho, A. G., Gerstenecker, C., Fernández, J., & Suyanto, I. (2005). Modeling the density at Merapi volcano area, Indonesia, via the inverse gravimetric problem. *Geochemistry, Geophysics, Geosystems*, *6*(9), Q09011. https://doi.org/10.1029/2005GC000986

Um, J., & Thurber, C. H. (1987). A fast algorithm for two-point seismic ray tracing. *Bulletin of the Seismological Society of America*, *77*(3), 972–986. https://doi.org/10.1785/BSSA0770030972

Voight, B., Constantine, E. K., Siswowidjoyo, S., & Torley, R. (2000). Historical eruptions of Merapi Volcano, Central Java, Indonesia, 1768–1998. *Journal of Volcanology and Geothermal Research*, 100(1–4), 69–138. https://doi.org/10.1016/S0377-0273(00)00134-7

article in press

Wagner, D., Koulakov, I., Rabbel, W., Lühr, B.-G., Wittwer, A., Kopp, H., Böhm, M., Asch, G., & MERAMEX Scientists. (2007). Joint inversion of active and passive seismic data in Central Java. *Geophysical Journal International*, *170*(2), 923–932. https://doi.org/10.1111/j.1365-246X.2007.03435.x

Walsh, B., Jolly, A. D., & Procter, J. (2017). Calibrating the amplitude source location (ASL) method by using active seismic sources: An example from Te Maari volcano, Tongariro National Park, New Zealand. *Geophysical Research Letters*, *44*(8), 3591–3599. https://doi.org/10.1002/2017GL073000

Young, K., Voight, B., Subandriyo, Sajiman, Miswanto, & Casadevall, T. J. (2000). Ground deformation at Merapi volcano, Java, Indonesia: Distance changes, June 1988–October 1995. *Journal of Volcanology and Geothermal Research*, *100*(1–4), 233–259. https://doi.org/10.1016/S0377-0273(00)00139-6

Zheng, Y., Xie, Y., & Long, X. (2021). A comprehensive review of Bayesian statistics in natural hazards engineering. *Natural Hazards*, *108*(1), 63–91. https://doi.org/10.1007/s11069-021-04729-2

Zhu, J., Chen, X., & Wen, L. (2021). Maximum covariance direction method for unconventional seismic sources. *Geophysical Journal International*, *227*(2), 813–831. https://doi.org/10.1093/gji/ggab232

Zobin, V. M. (2016). *Introduction to volcanic seismology* (3rd ed.). Elsevier.

article in press